A national laboratory of the U.S. Department of Energy
Office of Energy Efficiency & Renewable Energy

National Renewable Energy Laboratory

Innovation for Our Energy Future

Studies of Basic Electronic Properties of CdTe-Based Solar Cells and Their Evolution During Processing and Stress

Annual Technical Report
1 November 2005 — 31 October 2006

J. Beach, F.H. Seymour, V.I. Kaydanov, and T.R. Ohno
Colorado School of Mines
Golden, Colorado

Subcontract Report
NREL/SR-520-41097
January 2007

NREL is operated by Midwest Research Institute • Battelle Contract No. DE-AC36-99-GO10337

Studies of Basic Electronic Properties of CdTe-Based Solar Cells and Their Evolution During Processing and Stress

Annual Technical Report
1 November 2005 — 31 October 2006

J. Beach, F.H. Seymour, V.I. Kaydanov, and T.R. Ohno
Colorado School of Mines
Golden, Colorado

NREL Technical Monitor: Harin S. Ullal

Prepared under Subcontract No. ADJ-2-30630-05

Subcontract Report
NREL/SR-520-41097
January 2007

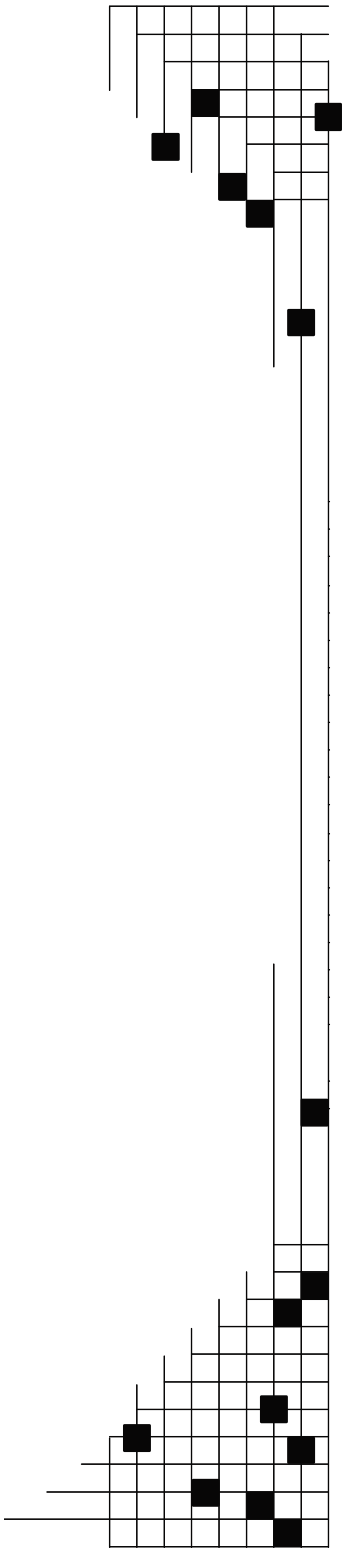

National Renewable Energy Laboratory
1617 Cole Boulevard, Golden, Colorado 80401-3393
303-275-3000 • www.nrel.gov

Operated for the U.S. Department of Energy
Office of Energy Efficiency and Renewable Energy
by Midwest Research Institute • Battelle

Contract No. DE-AC36-99-GO10337

PREFACE

This report presents the CSM Team activities for the period (1 November 2005-31 October 2006) under the extension of the subcontract ADJ-2-30630-05, "Studies of Basic Electronic Properties of CdTe-based Solar Cells". The tasks for the continuing studies in the project extension were defined as follows:

Task 1. Study of deep electronic states controlling Voc in CdTe/CdS thin film solar cells

Task 2. Test different cell growth approaches that can lead to higher Voc in these cells.

In our preceding studies in this project (see Final 2005 Report to NREL), combined admittance spectroscopy (AS) and capacitance transients (CTr) measurements were used to detect and characterize numerous deep electronic states (DES) in thin film CdTe/CdS cells. The AS approach was applicable to the DES with the characteristic trap times, τ_t, in the range of $10^{-2} s \ \ to \ \ 10^{-7} s$. The CTr measurements extended available the characteristic time range to minutes, hours and even days. A new measurement system was developed that permitted frequency- and bias-dependent admittance measurements in a wide range of temperatures. In addition, we could measure very long transients (up to tens of hours) at a fixed and very stable temperature.

AS/CTr measurements and the data analysis led to important and sometimes unexpected results. Among the latter were:

(a) Concentrations of detected traps, N_t, in CdTe cells fabricated at different facilities are rather high, exceeding "doping level" commonly determined with the C-V profiling, N_{C-V}. That makes application of common approaches to AS, DLTS and C-V data analysis based on the assumption of low relative trap density questionable. In particular, the trap concentration (from AS and DLTS) is underestimated while the doping level derived from C-V measurements can be strongly overestimated.

(b) Changes in processing that diminish cell efficiency often are accompanied with reduced estimated trap concentration.

The AS and CTr measurements in a temperature range of -190^0C to ~ $+80^0$C were performed on CdTe cells subjected to various combinations of $CdCl_2$ treatment and doping with Cu (the cells were provided by Dr. D. Albin (NREL)). These studies revealed traps for majority

carrier holes, as well as for minority electrons with activation energy varying from 0.13 eV to ~0.8 eV and apparent capture cross sections varying by four orders of magnitude. Manifestations of particular traps in as-prepared cells, specifically their concentrations, as well as their behavior under stress were influenced by variations in $CdCl_2$ treatment and Cu doping.

This report presents the results of the continued studies of DES (Task 1), including:
(a) analysis of the factors that affect the trap signatures derived from AS and CTr measurements, such as activation energy capture cross sections, as well as the trap density estimates
(b) comparative studies of the cells received from four different sources and prepared with significant variations in the cell structure and processing procedures

In our previous report we presented and discussed our activities in the cell processing aimed at improvement of the cell performance. Basic deposition techniques in use were:

- Chemical bath deposition for CdS layer
- Electrodeposition and gas transport deposition for CdTe
- Thermal evaporation for the back contact structure: Cu/ZnTe/gold

Deposited layers were subjected to various post-deposition treatments including:

- Anneal of CdS with and without $CdCl_2$ prior to the CdTe deposition
- CdTe postdeposition treatment with $CdCl_2$
- Cu/ZnTe postdeposition annealing

This report presents continuing studies aimed at the processing improvement and optimization (task 2). This time the only CdTe deposition method was gas transport deposition with the "Gas-Jet" system designed and developed at CSM. For CdS we added thermal evaporation. Since the performance of the cell was sensitive to the contact annealing stage, the post -Cu/ZnTe anneal was optimized. These and other modifications of the processing procedure led to improvement of the cell performance, in particular to increase of open circuit voltage, V_{OC}. The best cell grown on the tin oxide coated soda lime glass without front contact buffer, demonstrated an efficiency of 12.6% (not NREL verified).

TABLE OF CONTENTS

LIST OF FIGURES

LIST OF TABLES

1. FUNDAMENTALS OF ADMITTANCE CHARACTERZATION TECHNIQUES

1.1. Basic Equations

1.1.1 Admittance spectroscopy.

A small amplitude (10mV) AC signal is applied to the device over a range of frequencies f and the admittance Y and phase angle θ are recorded. From these the p-mode (parallel equivalent circuit of capacitor and resistor) capacitance C_p and conductance G_p are calculated as:

$$C_p = \frac{\mathrm{Im}(Y)}{2\pi f} = \frac{Sin(\theta)|Y|}{2\pi f},\ G_p = \mathrm{Re}(Y) = Cos(\theta)|Y| \qquad (1.1)$$

At sufficiently low frequencies and high temperatures the electrical charges for the traps near the "crossing point" (Fermi, E_F, and DES energy, E_t, levels are crossing) follow the AC voltage oscillations and directly contribute to the measured capacitance and AC conductance. At high frequencies or low temperatures these trap charges cannot follow the AC signal resulting in a lower measured capacitance and saturation in the $G_p(\omega)$ dependence. The parallel mode capacitance $C_p(\omega)$ and conductance $G_p(\omega)$, as a function of the AC signal angular frequency $\omega = 2\pi f$ are given by [2]:

$$C_p(\omega) = C_d + \frac{C_t^0}{1+(\omega/\omega_t)^2},\ G_p(\omega) = G_d + \frac{G_t^o(\omega/\omega_t)^2}{1+(\omega/\omega_t)^2},\ G_t^0 = C_t^0\omega_t, \qquad (1.2)$$

where C_d and G_d represent the *diode* capacitance and conductance in the absence of traps, and $C_t^0 = C_t(\omega \to 0)$ and $G_t^0 = G_t(\omega \to \infty)$ are the maximum additional capacitance and conductance resulting from the traps; ω_t is the angular characteristic frequency, inverse of the trap characteristic time, τ_t. Figure 1.1 illustrates the capacitance and conductance as a function of frequency.

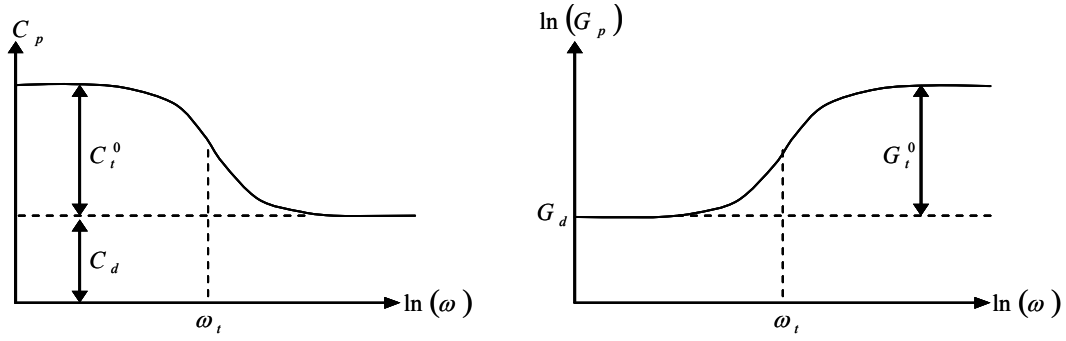

Figure 1.1. Capacitance C_p and conductance G_p as a function of AC frequency. C_d and G_d are the depletion region contributions; $C_t^0(\omega)$ and $G_t^0(\omega)$ are the trap contributions to the capacitance and conductance.

The characteristic frequency ω_t corresponds to the inflection points of maximum slope and can be estimated based on Equations (1.3) or (1.4):

$$\omega_t = \omega_{peak} \ \ for \ \ \frac{dC_p(\omega)}{d\ln(\omega)} \ \ and \ \ \frac{G_p(\omega)}{\omega} \tag{1.3}$$

$$\omega_t = \sqrt{3}\,\omega_{peak} \ \ for \ \ \frac{dC_p(\omega)}{d\omega} \ \ and \ \ \frac{dG_p(\omega)}{d\omega} \tag{1.4}$$

This approach works well when there is a single DES level that stands out.

Characteristic frequency is determined by the electron and hole capture (c) and emission (e) rates:

$$\omega_t = \tau_t^{-1} = c_p + e_p + c_n + e_n \tag{1.5}$$

For holes

$$c_p = \sigma_p v_p N_v \exp[-(E_F - E_V)/k_B T \tag{1.6}$$

$$e_p = \sigma_p v_p N_v \exp[-(E_t - E_V)/k_B T \tag{1.7}$$

where σ_p is the hole capture cross section, v_p is the hole thermal velocity, N_v is the valence band effective density of states, and E_F, E_t and E_V are the Fermi, DES, and valence band edge energy levels, respectively. The equations are similar for the electron capture and emission rates, with respect to the conduction band.

1.1.2 Capacitance transients

If a perturbation is applied to the diode electron system, such as light or electrical bias, E_F shifts with respect to E_t, and the trap occupancy n_t changes to a new steady state level. When the perturbation is removed at the time moment $t = 0$, n_t relaxes from this steady state level $n_t(t = 0)$ back to the initial equilibrium level $n_t(t = \infty)$. For a single level DES, assuming that the process is reversible and that there are no meta-stable states, this occurs according to the exponential equation:

$$n_t(t) = n_t(\infty) - (n_t(\infty) - n_t(0))\exp(t/\tau_t), \tag{1.8}$$

where $\tau_t = \omega_t^{-1}$ is a characteristic time dominated by the largest value for c_n, e_n, c_p or e_p.(1.5). Correspondingly the CTr is described by the equation

$$C_p(t) = C_d + C_t^0 \exp(-t/\tau), \tag{1.9}$$

The characteristic time τ can be determined by looking for peaks in $\frac{dC_p(t)}{d\ln(t)}$ where $\tau = t_{peak}$.

1.2 Stretched Exponential Parameter β

The AS and CTr experimental data frequently did not adequately fit the basic equations above. A much better fit was found with the addition of a phenomenological stretched exponential parameter β in the basic capacitance equation. The modified equation becomes:

$$C_p(\omega) = C_d + \frac{C_t^0}{1 + \left((\omega/\omega_t)^2\right)^{\beta}} \tag{1.10}$$

Figure 1.2 shows the AS curves for experimental data from a CdTe solar cell, a model fit with $\beta = 0.5$, and a model fit with β=1.

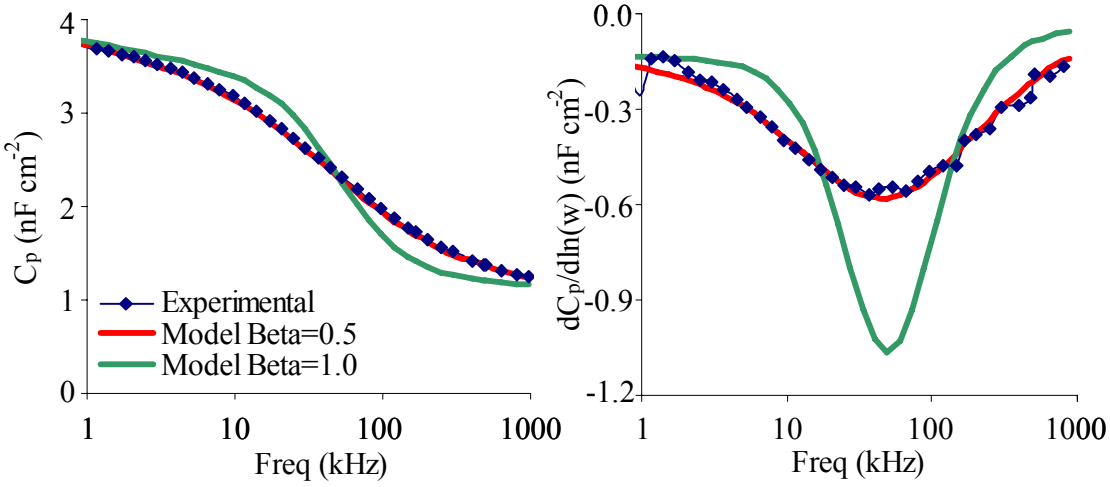

Figure 1.2 Admittance Spectroscopy example showing goodness of fit with phenomenological parameter β=0.5.

Mathematical analysis shows that the $\omega_t = \omega_{peak}$ relationship is independent of the β parameter, and there is no need to change the procedure of the ω_t determination from $dC_p / d\ln t$.

The value of C_t^0 can be determined from the peak magnitude:

$$C_t^0 = -\frac{2}{\beta} \times (Peak - Magnitude) \tag{1.11}$$

Distortion of the AS spectrum that results in a better fit with stretched exponential dependence can be explained by the DES band, rather than a discrete level. Another possibility is a high density of a discrete level DES that causes Fermi level pinning and band bending in such a way that the AS signal is distorted. Simulations with the SCAPS software package indicate that this is a plausible explanation (see Section 2).

The capacitance transient experimental curves are also better described with the stretched exponential equation:

$$C_p(t) = C_d + C_0 \exp\left(-(t/\tau)^{\beta}\right) \tag{1.12}$$

Similarly to AS, the $\omega_t = \omega_{peak}$ relationship in $dC_p / d\ln\omega$ is independent of the β parameter.

The C_t^0 value can be determined from the peak magnitude as:

$$C_t^0 = -\frac{e}{\beta} \times (Peak - Magnitude), \tag{1.13}$$

where $e = \exp(1) = 2.718$.

Similarly to AS, a good fit to the experimental data is often found with $\beta \sim 0.5$.

1.3 Temperature Dependence of Characteristic Frequency/Characteristic Time

The trap characteristic frequency is related to the capture and emission rates and therefore dependent on both Fermi and DES energy levels (see Eqs. (1.5)-(1.7)). As mentioned above the recharging of traps located near the crossing point dominates the frequency dependent component of measured admittance. Since at this point $E_t = E_F$, capture and emission rates for the majority carriers are equal to each other and have the same temperature dependence, hence for holes

$$\omega_t = \tau_t = 2\sigma_p v_p N_v \exp[-(E_t - E_V)/k_B T] \qquad (1.15)$$

Below we show three different representations of the temperature dependent AS spectra. Exponential dependence ω_t(T) is illustrated by Fig. 1.3. It plots C_p versus frequency (left graph) and $dC_p/d\ln\omega$ vs. frequency (right graph) for a range of fixed temperatures. The increase of ω_t with temperature can be seen with minima that correspond to ω_t on the $dC_p/d\ln\omega$ vs. frequency graph.

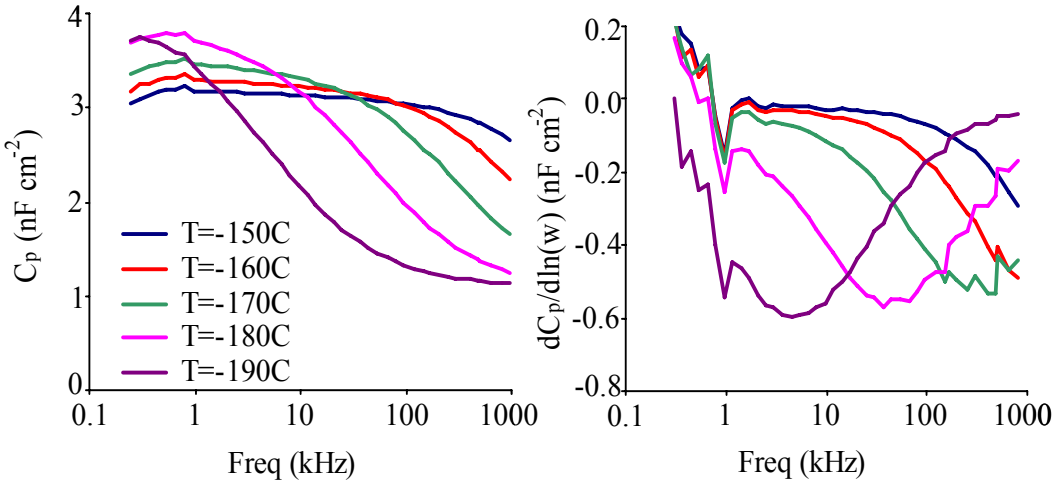

Figure 1.3 C_p and $dC_p/d\ln(\omega)$ vs. AC frequency at different temperatures for a CdTe solar cell.

This representation can become crowded and difficult to interpret in a case of wide range of temperatures and multiple DES detected. One alternative is to graph AC conductance G_p versus temperature at fixed frequencies ω. An example is shown in figure 1.4 for a CdTe solar cell with frequencies ranging from 1MHz (red line at top) down to 1 kHz (bottom line). The local peaks on the lines indicate a DES with the characteristic frequency ω_t corresponding to the fixed line frequency ω at the peak's temperature T_{peak}. In this example two DES outlined in blue are clearly visible as is the increasing ω_t with temperature.

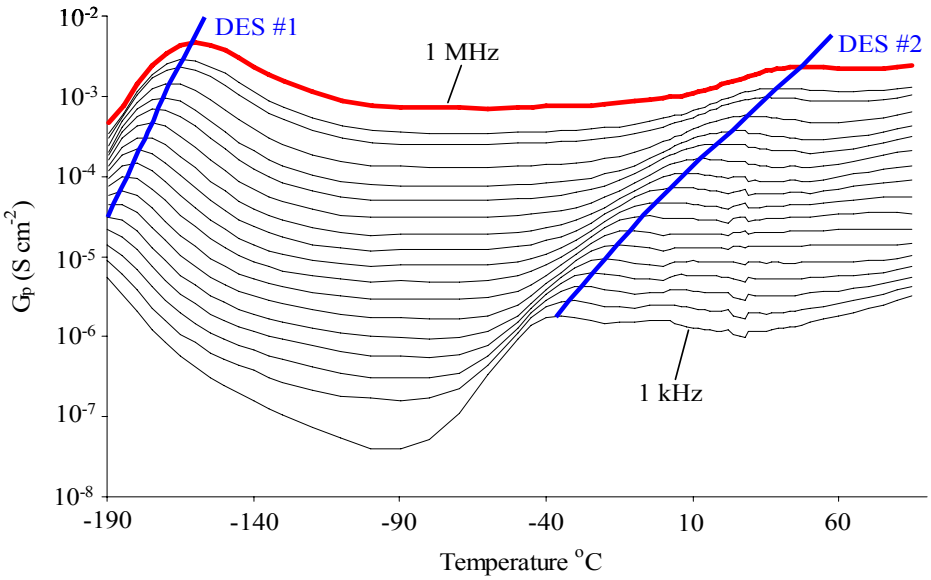

Figure 1.4. Conductance G_p versus temperature for a range of frequencies. The top red line corresponds to 1 MHz and the bottom line corresponds to 1 kHz. The blue lines highlight peaks from two DES with different $\omega_t(T)$.

Another alternative is to graph C_p versus T at fixed f. Figure 1.5 shows the same CdTe solar cell with frequencies ranging from 1 MHz (bottom line) to 1 kHz (top line). Here the DES can be seen as a spread in C_p values over f. The low temperature DES #1 (-190^{o}C to ~ -100^{o}C) is easily seen. The mid temperature DES #2 (-40^{o}C to 30^{o}C) is less obvious but can be seen as a kink in the lines. At warmer temperatures (30^{o}C and above), the nearly constant spread in C_p values at different f indicates a continuous band of DES energy levels.

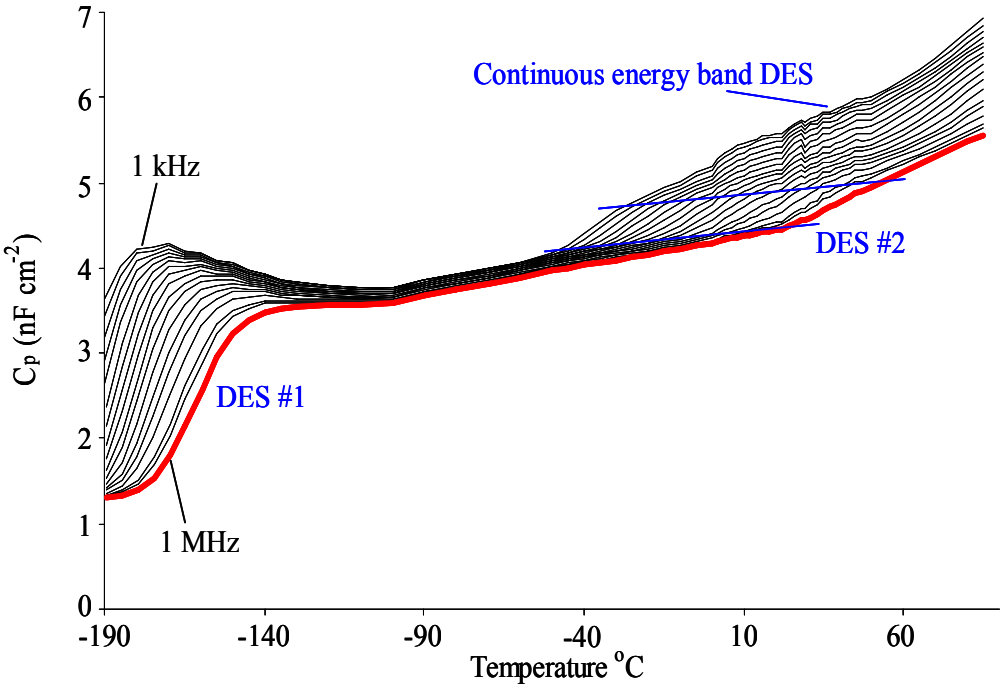

Figure 1.5 Capacitance C_p versus temperature for a range of frequencies. The bottom red line corresponds to 1 MHz and the top line corresponds to 1 kHz.

In the temperature range -170°C to -100°C the low frequency capacitance (top lines) decreases in magnitude with increasing temperature. This behavior contradicts with Eq. (1.1). In Sec.2, using simulations with SCAPS we will show that this effect can be explained by a steep defect concentration gradient near the back contact combined with the back contact Schottky barrier. As E_F rises with increasing T, it crosses E_t at different locations of decreasing density of the defect.

Figure 1.6 illustrates typical evolution of capacitance C_p transients with temperature for the bias sequence: 30 s at zero bias, 300 s at forward bias +0.5 V, and a 300 s recovery period at zero bias. The minima in the $\frac{dC_p(t)}{d\ln t}$ graph to the right shows reducing τ with increasing T.

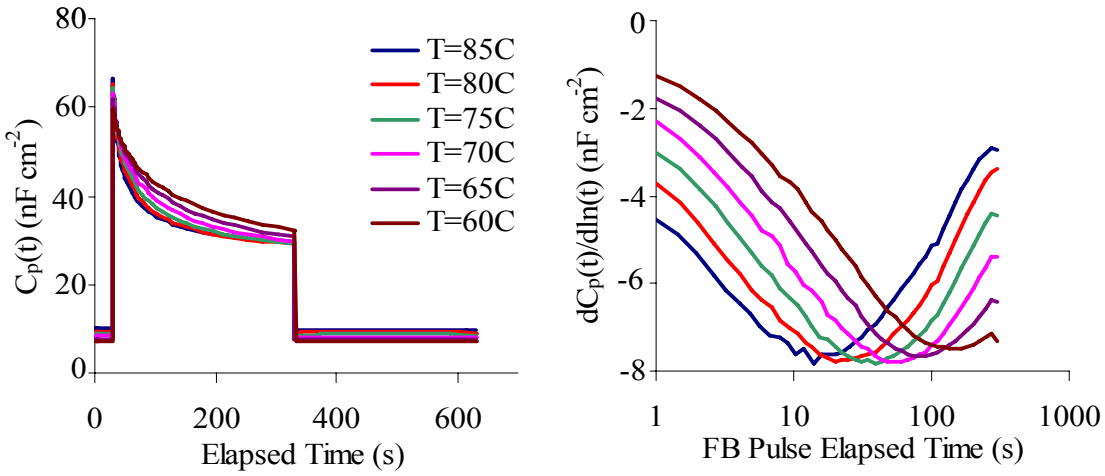

Figure 1.6. CTr measurements on CdTe cell. $C_p(t)$ versus t for the complete transient cycle (left) and $\frac{dC_p(t)}{d\ln(t)}$ versus $\ln(t)$ for the forward bias +0.5V pulse (right).

1.4 Estimating E_a and σ_a with Arrhenius Plot

Since in Eq. (1.15) $v_T \propto T^{1/2}$ and $N_V \propto T^{3/2}$, the characteristic time τ dependence on T is linear on an Arrhenius plot of the form $\ln[(\tau T^2)^{-1}]$ versus $1000/T$. A linear regression is used to estimate the activation energy E_a and apparent capture cross section σ_a as:

$$E_a = -1000 \times Slope \times k_b \tag{1.16}$$

$$\sigma_a = \frac{\exp(Y_i)}{3.00x10^{21}(m^*/m_o)} \tag{1.17}$$

where $Slope$ is the regression line slope, Y_i is the regression line y-intercept at $T = \infty$, and m^*/m_o is the charge carrier's relative effective mass. The activation energy approximation $E_a \approx \Delta G$ is often assumed while more precisely $E_a = \Delta H + E_\sigma$, where ΔG is the Gibbs free energy, ΔH is the enthalpy, and E_σ is the potential barrier for carrier capture by a trap. Also, the apparent capture cross-section approximation $\sigma_p \approx \sigma_a$ is often made whereas more precisely,

$\sigma_a = \chi_n \sigma_\infty$, where σ_p is the capture cross section at T of measurements, $\sigma_\infty = \lim_{T\to\infty} \sigma(T)$, and χ_n is the entropy factor for the thermal emission.

Meyer-Neldel Rule behavior

A group of $\{E_a, \sigma_a\}$ DES signatures determined by Arrhenius regression are said to obey the Meyer Neldel Rule (MNR) [3] when they form a straight line on a E_a vs. $\ln(\sigma_a)$ plot, referred to as a Meyer-Neldel plot. This relationship indicates the same underlying DES in spite of a wide range of E_a and σ_a values. This allows for the grouping of observed $\{E_a, \sigma_a\}$ data points into DES "families" and simplifies classification of DES and identification of underlying defects. A number of possible explanations for MNR behavior have been proposed [4]. Early in this study, significant MNR behavior was observed with DES detected with CTr. It was mostly caused by instrumentation noise and aggravated by the narrow T range where a specific trap is detectable. Subsequent improvements to the measurement system expanded the range of τ and consequently T, reducing this effect.

1.5 Estimating Trap Concentrations from Capacitance Measurements

Knowledge of the DES concentration is helpful in evaluating their impact on solar cell performance. The simple theory for a single trap level with uniform distribution of trap concentration N_t and "doping level" N, provides an equation [2]:

$$\frac{C_t^o}{C_d} = \frac{N_t}{N} \frac{1 - x_t / x_d}{1 + (N_t / N) \cdot (x_t / x_d)} \tag{1.18}$$

where x_d is the depletion width and x_t is the "crossing point" - the distance from the interface to the point where the trap level crosses the Fermi level: $E_t(x_t) = E_F$. Eq. (1.18) is derived under assumption of low trap concentration. In the case of $N_t << N$, Eq. (1.18) takes a simpler form:

$$\frac{C_t^o}{C_d} = \frac{N_t}{N}\left(1 - \frac{x_t}{x_d}\right) = \frac{N_t}{N}\left(\frac{U_t}{U}\right)^{1/2} \tag{1.19}$$

where $U = V_{b-i} + V_{bias}$ is the total band bending and $U_t \equiv (E_t - E_F)/e$. If to assume also $x_t / x_d << 1$ (e.g., at forward bias applied), the equation transforms further to $C_t^o / C_d \approx N_t / N$. If one observes $C_t^o / C_d \geq 1$, that means that the trap density is higher than the "doping level". Indeed, sometimes we have observed a two- to three-fold decrease in capacitance value with increasing frequency. In this case the simple theory does not work.

If trap concentration is high and $N << N_t$, the Fermi level may be pinned by the trap level E_t. The influence of this effect was simulated with SCAPS and is discussed in Section 2. Additional problem comes from the uncertainty in spatial distribution of N_t, or both N and N_t, and corresponding uncertainty in space charge density and electric potential distribution. Rather than make definite estimates of trap concentrations from capacitance measurements, we make the relative estimates of N_t for different DES and differently processed cells based on the C_t^0 values derived using Eqs. (1.11) and (1.14). The same approach is used to see trends in the particular trap/defect concentration changes due to the cell stressing.

2. SCAPS SIMULATION

The SCAPS package [5] allows a solar cell to be modeled with up to three DES with known E_a, σ_a, and N_t. The simulated AS results can be compared to experimental data and help validate or discredit different working hypotheses about the DES system.

Two SCAPS CdTe solar cell models are discussed in this section to illustrate how simulations can help explain experimental observations. The first model shows that with a combination of a steep DES concentration gradient near the back contact, a back contact Schottky barrier, and high DES concentration relative to the doping level, AS results can show a decreasing capacitance with increasing temperature. The second model shows how the magnitude of an AS signal can be impacted by the cell width and how Fermi level pinning can distort the calculated activation energy and cause non-exponential behavior.

2.1 DES Concentration Gradient

A number of experimental AS results in this study have shown decreasing capacitance magnitudes with increasing temperature as was seen in Figure 1.5 for the low frequency capacitance (upper line) at T<-100^{o}C. These results are counter-intuitive since the increasing temperature leads to ionization of deeper states, which increases the space charge density and reduces the depletion width resulting in a higher measured capacitance. However, the SCAPS simulation shows that a combination of three conditions can cause this unexpected result observed experimentally.

(a) The DES concentration has a gradient near the back contact. When modeling, we used $E_a = 0.15eV$, simulating cadmium vacancies V_{Cd}^{-}; the concentration was set to N_t=3x10^{19}cm^{-3} at the back contact and decreased exponentially to 3x10^{14}cm^{-3} over a length of about 35nm. This N_t gradient is reasonable since the cell post deposition NP etch is known to create a tellurium rich layer at the back contact.

(b) There is a back contact Schottky barrier. The barrier height was set to Φ_b = 0.5eV with respect to Fermi level. With this, when the Fermi level rises with increasing temperature, the V_{Cd} crossing point will shift in the near-back contact region with a steep N_t gradient.

(c) The shallow acceptor concentration is much lower than the DES concentration. This causes Fermi level pinning at the DES level and amplifies the AS signal. The shallow acceptor concentration was set to $N_a=10^{12}\text{cm}^{-3}$. This is plausible if V_{Cd} is taken as the primary dopant for the CdTe layer. The rest of the parameters are typical values for CdTe solar cells and were selected from two sources [6, 7].

Band diagrams for this model at -190°C and -100°C are shown in figure 2.1.

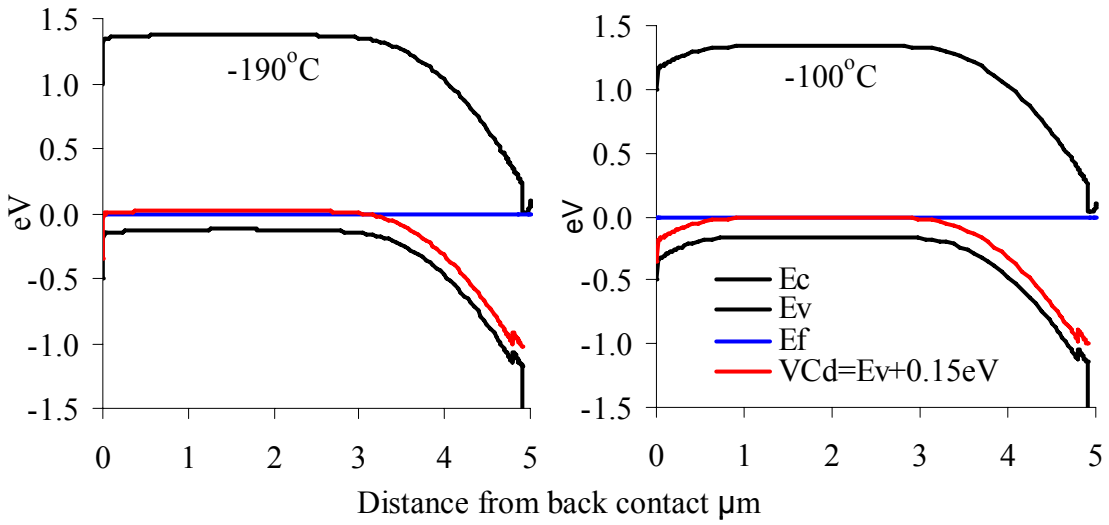

Figure 2.1 Band diagrams for SCAPS model at -190°C and -100°C. The conduction and valence bands are in black, the Fermi level in blue, and the V_{Cd} DES in red.

At -190°C the Fermi level is pinned to the V_{Cd}^{-} level almost all of the way to the back contact. The pinning near the back contact where the V_{Cd}^{-} concentration is high greatly enhances the AS signal. However, at -100°C, due to the Schottky barrier band bending, the higher Fermi level is no longer pinned to the V_{Cd}^{-} level in the vicinity of the back contact. The crossing point shifts to the region of much lower V_{Cd}^{-} concentration and the AS signal is significantly reduced.

The SCAPS simulated AS C_p versus T diagram is shown in figure 2.2. The decreasing low frequency capacitance with increasing temperature is evident in the temperature range -170°C to -120°C. The effect observed experimentally (see Fig. 1.5) is smaller than in this simulated example but qualitatively is the same.

The presence of a Schottky barrier manifested itself as an AS signal in the temperature range -80°C to 40°C. This illustrates how the back contact barrier can be mistaken for a DES. In simulations the back barrier has consistently had $\beta = 1$. There is an unexplained kink in the capacitance values measured between 5°C and 10°C. It is likely that this is an artifact of the software and is caused by numerical calculation problems.

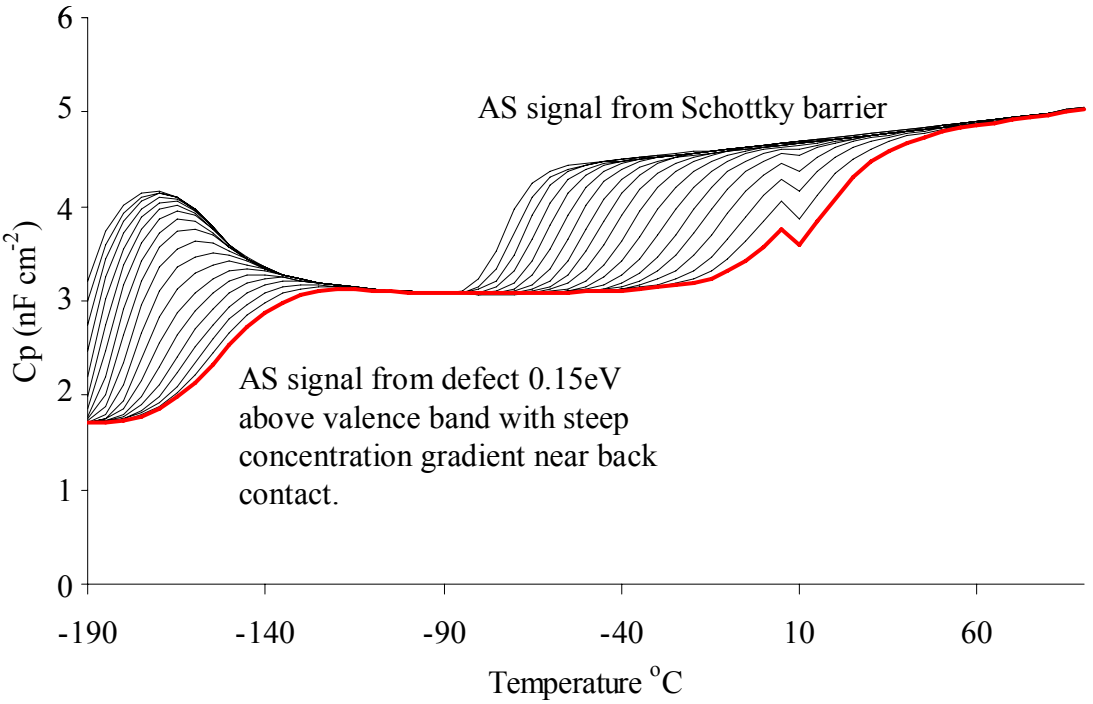

Figure 2.2 SCAPS simulated C_p versus T graph for a range of frequencies. The bottom red line corresponds to 1 MHz and the top line corresponds to 1 kHz.

2.2 Fermi Level Pinning, Distorted E_a and Non-Exponential Behavior

The simulation examples in this section examine the two cells that are identical except for the CdTe layer thickness, 8μm for cell A and 3μm for cell B. We start with the band diagrams and show how the characteristic frequency as a function of distance from the back contact is different for the two cells. This difference alters the AS signal from each cell and leads to differences in the calculated values for E_a, σ_a, and β.

The band diagrams for the two cells are shown in Figure 2.3 for $T = -170^{o}C$. There is a DES in the model with $E_a = 0.15eV$, $\sigma_a = 2x10^{-14}cm^2$, and $N_t = 3x10^{14}cm^{-3}$. There is a low shallow acceptor with concentration of $N_a = 10^{12}cm^{-3}$.

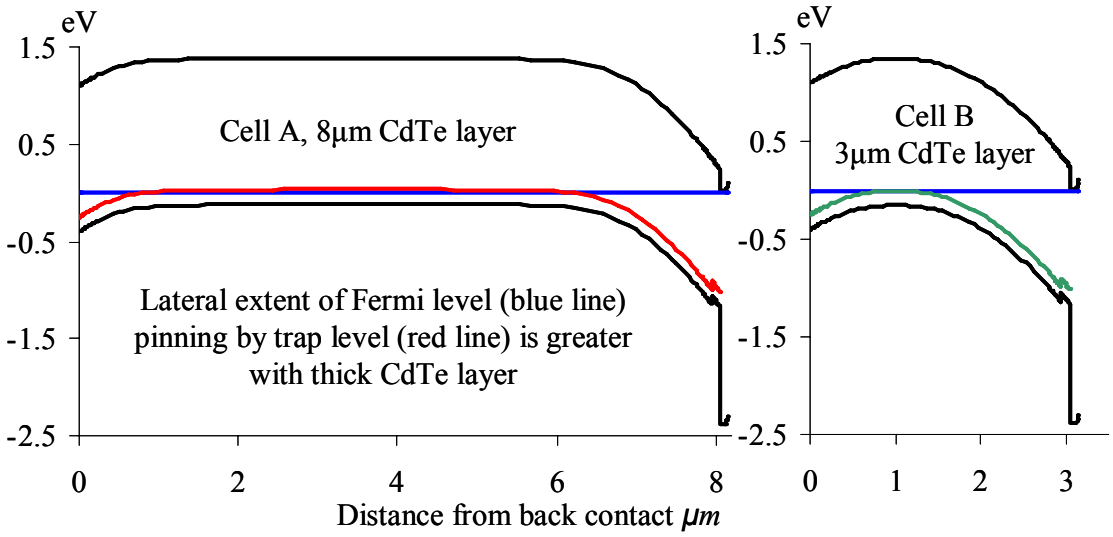

Figure 2.3 SCAPS simulation band diagrams for CdTe solar cells at T=-170°C showing Fermi level (blue line) and pinning by high concentration trap level (red line) for cell A with 8 µm CdTe layer (left) and green line for cell B with 3 µm CdTe layer (right).

The acceptor-type DES level is fixed at $E_t - E_V = 0.15eV$ while the Fermi level $E_F - E_V$ varies as a function of the free carrier concentration at different distances from the back contact. Knowing the Fermi level, we can calculate the free hole concentration as a function of distance from the back contact with equation $p = N_V \exp\left(\frac{-(E_F - E_V)}{k_b T}\right)$. Figure 2.4 (left) shows an expanded scale band diagram view of the acceptor DES energy level for the 8 µm and 3 µm cells with respect to the Fermi level. Figure 2.4 (right) shows the free majority carrier (hole) concentrations for the 8 µm and 3 µm cells as a function of distance from the back contact. The back contact and main junction depletion regions are evident from the low free carrier concentrations at both ends of the cells. The 3µm cell is nearly fully depleted across the CdTe layer. The 8µm cell has a free carrier concentration that exceeds the shallow defect doping

concentration of $N_d = 10^{12} cm^{-3}$ in the central quasi-neutral or "non-depleted" region. The ionized DES is the source of these free carriers.

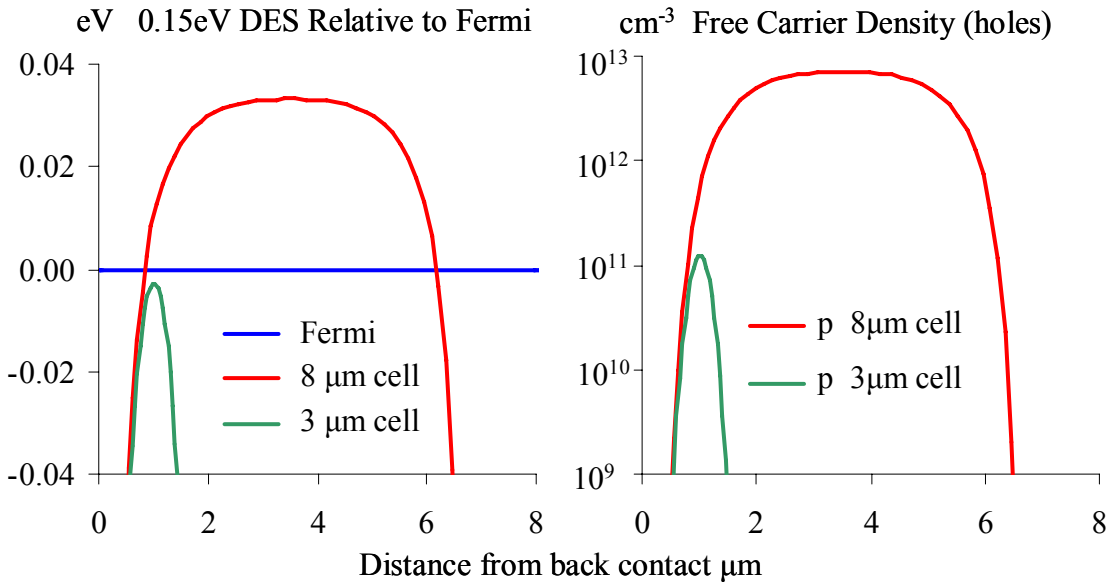

Figure 2.4 SCAPS simulated 8 µm and 3 µm cells for T=-170°C. DES energy levels relative to Fermi level (left). Free carrier density (right).

With the free carrier density known, it is possible to determine the DES capture rate for each DES as a function of distance from the back contact, using equations $c_p = \sigma_p v_p p$, and $e_p = \sigma_p v_p N_v \exp\left(\frac{-(E_t - E_V)}{k_b T}\right)$. Since $E_t - E_V = const$, the emission rate will be constant as a function of distance from the back contact. With the emission and capture rates known, the ionization of the DES can be determined from equation $\frac{n_t}{N_t} = \frac{e_p}{e_p + c_p}$. Figure 2.5 (left) shows the hole capture and emission rates for the 8 µm and 3 µm cells as a function of distance from the back contact. Figure 2.5 (right) shows the ionized DES concentration n_t as a function of distance from the back contact.

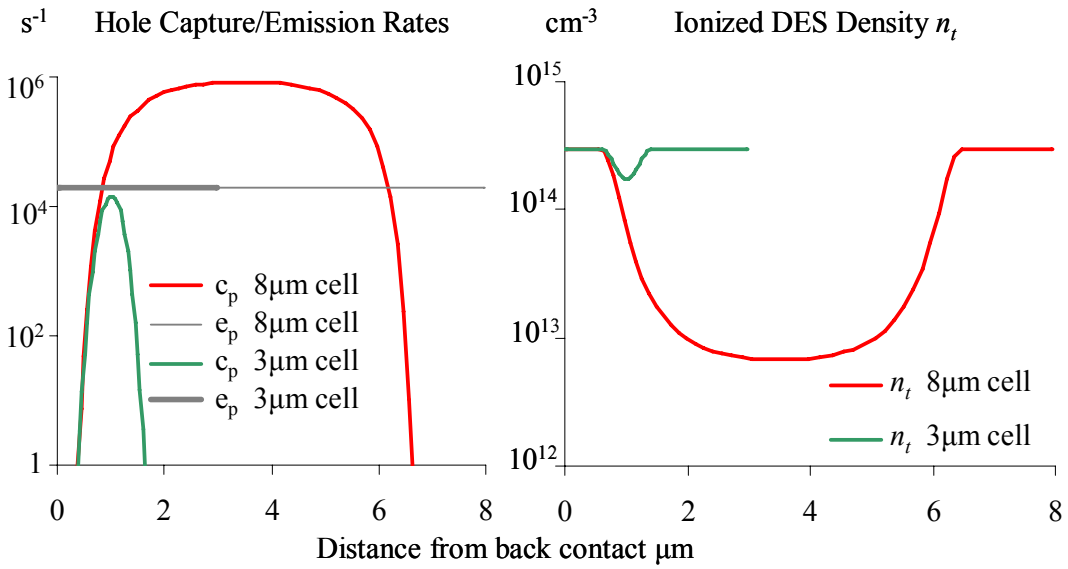

Figure 2.5 SCAPS simulated 8 µm and 3 µm cells. Hole capture and emission rates (left) and ionized DES density (right).

As expected, when the DES level is significantly below the Fermi level, the DES are fully ionized (occupied with electrons) with $n_t \approx N_t = 3x10^{14} cm^{-3}$. For the 8µm cell, in the quasi neutral central region, the ionized DES density approaches that of the free carrier density seen in figure 2.4 as a further indication that they are the dominant source of free carriers.

The capture density of holes by the DES is the product of the DES hole capture rate c_p and concentration of DES available for capturing holes, that is n_t. The emission density of holes by the DES is the product of the DES emission rate e_p times the DES concentration available for emitting holes $N_t - n_t$. At equilibrium, the capture and emission densities are equal. When there is a small shift in the Fermi level such as that caused by a LCR meter AC signal, the change in charge will be proportional to this capture/emission density. Thus, the parts of the cell with the highest capture/emission densities will make the greatest contributions to the measured capacitance.

Knowing the hole emission and capture rates it is possible to calculate the characteristic time from equation $\tau^{-1} = c_n + e_n + c_p + e_p$ [2]. The electron capture and emission rates, c_n, e_n, are negligible because the DES energy level and p-type Fermi energy level are located far from the conduction band. Experimentally characteristic frequency $\omega_t = \tau^{-1}$ is determined as the LCR

meter angular frequency $\omega = 2\pi f$ at which $dC_p(\omega)/d\ln(\omega)$ has a peak. Figure 2.6 (left) shows the capture/emission densities for the DES as a function of distance from the back contact. Figure 2.6 (right) shows the DES characteristic frequencies f_t as a function of distance from the back contact. The latter shows that characteristic frequencies determined in this way are significantly different for cells of different thicknesses: $f_t \approx 10^5\ Hz$ for the 8 μm cell while $f_t \approx 5x10^3\ Hz$ for the 3 μm cell.

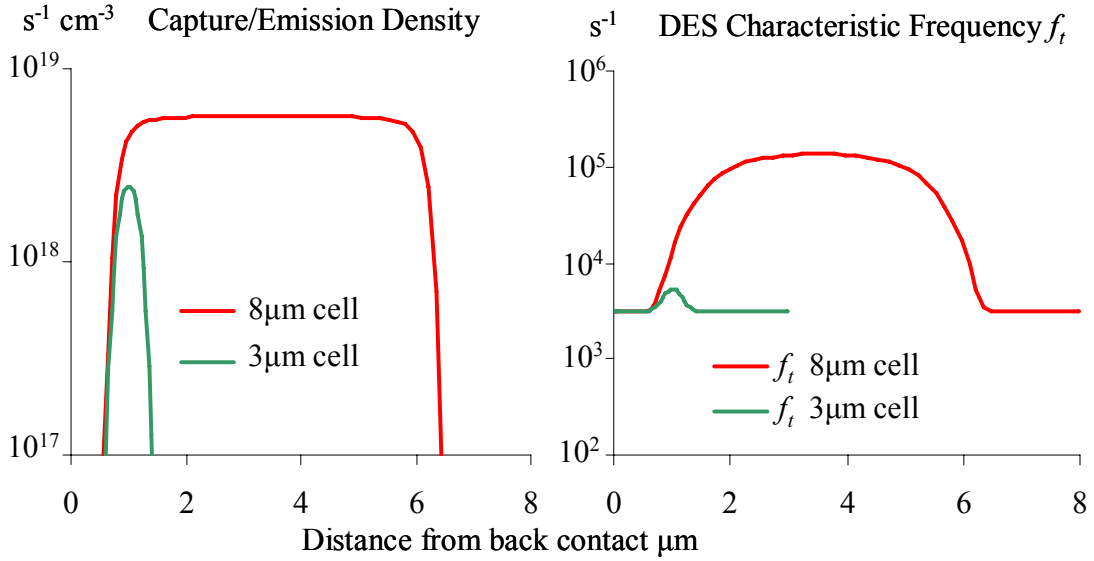

Figure 2.6 SCAPS simulated 8 μm and 3 μm cells. DES hole capture/emission density at equilibrium (left) and DES characteristic frequency f_t (right).

Figure 2.7 shows the SCAPS simulated frequency dependencies of C_p and $dC_p/d\ln(\omega)$. The C_p vs. f graph (left) shows that the 8μm cell has a larger magnitude $C_t^0 = 1.39nF\,cm^{-2}$ than that of the 3μm cell $C_t^0 = 0.18nF\,cm^{-2}$. This could be expected since in the former the region where E_t is very close to E_F is much thicker hence the number of DES contributing to the capacitance signal is much greater than in the thinner cell. This illustrates the complexity of estimates of N_t from the C_t^0 value. In our example of two cells with the same DES concentration N_t but different thicknesses, the C_t^0 values differ by a factor of ~8.

If the cell is sufficiently thin, it will be fully depleted and the DES level will not even approach the Fermi level making it undetectable with AS. This explains why cells produced by Colorado State University [7] that have a thin <2 μm CdTe layer had little or no detectable DES AS density (we do not present the data for these cells because the studies are not completed).

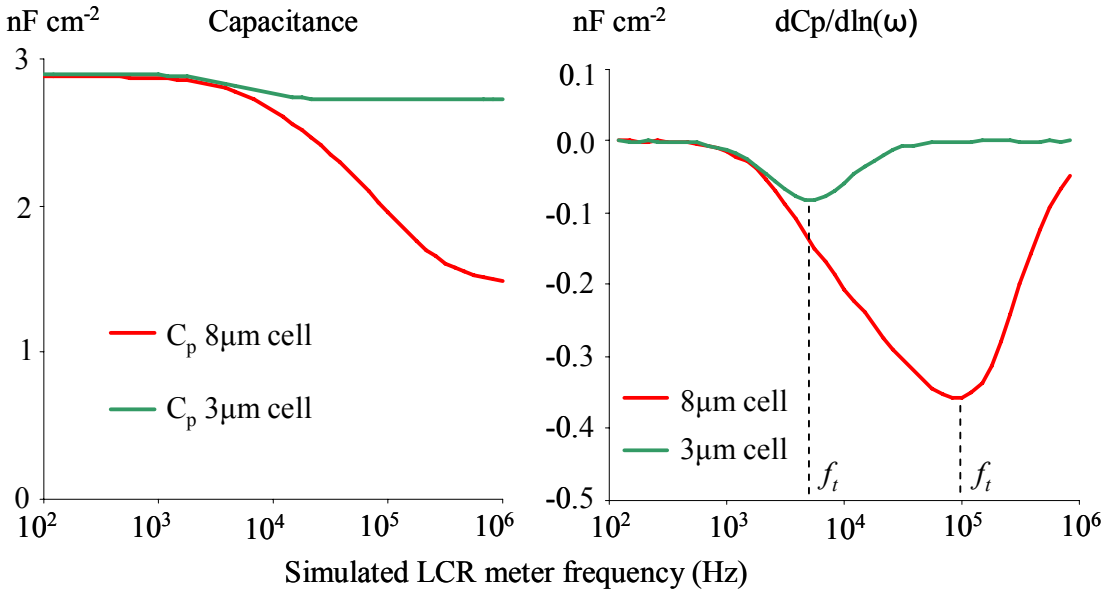

Figure 2.7 SCAPS simulated 8 μm and 3 μm cells at -170°C. C_p versus simulated AC signal frequency (left) and $dC_p/d\ln(\omega)$ versus simulated AC signal frequency (right).

The graph $dC_p/d\ln(\omega)$ vs. simulated AC signal frequency in figure 2.7 (right), makes evident the difference in the characteristic frequency minima. The 8μm cell has $f_t = 10^5\ Hz$ while the 3μm cell has $f_t = 5x10^3\ Hz$ corresponding to the dominant characteristic frequencies seen in figure 2.6 (right). This difference in f_t leads to differences in the $\tau(T)$ dependencies that cause distortions in the calculated values for E_a and σ_a. The $dC_p/d\ln(\omega)$ signal spread spans three decades from f~10^3 to f~10^6 Hz with the 8μm cell and only goes from 10^3 to 2x10^4 Hz with the 3μm cell. The larger spread with the 8μm cell is caused by the larger range of characteristic frequencies that contribute to the AS signal. This causes the stretched exponential behavior that leads to values of $\beta < 1$. The asymmetry that seen in the 8μm $dC_p/d\ln(\omega)$ curve is commonly observed in the experimental data.

The Arrhenius plot for the simulated 8μm (red) and the 3μm (green) cells with the single DES of $E_a = 0.15eV$, $\sigma_a = 2x10^{14} cm^2$ are shown in figure 2.8. For the 3μm cell, the Arrhenius regression indicates $E_a = 0.15eV$, $\sigma_a = 2x10^{14} cm^2$, $\beta = 0.94$ which is consistent with the input and $E_t \approx E_f$ where the capacitance signal is detected. For the 8μm cell, the Arrhenius regression indicates $E_a = 0.10eV$, $\sigma_a = 2x10^{15} cm^2$, $\beta = 0.45$ which shows the distortions to the regression slope that can occur.

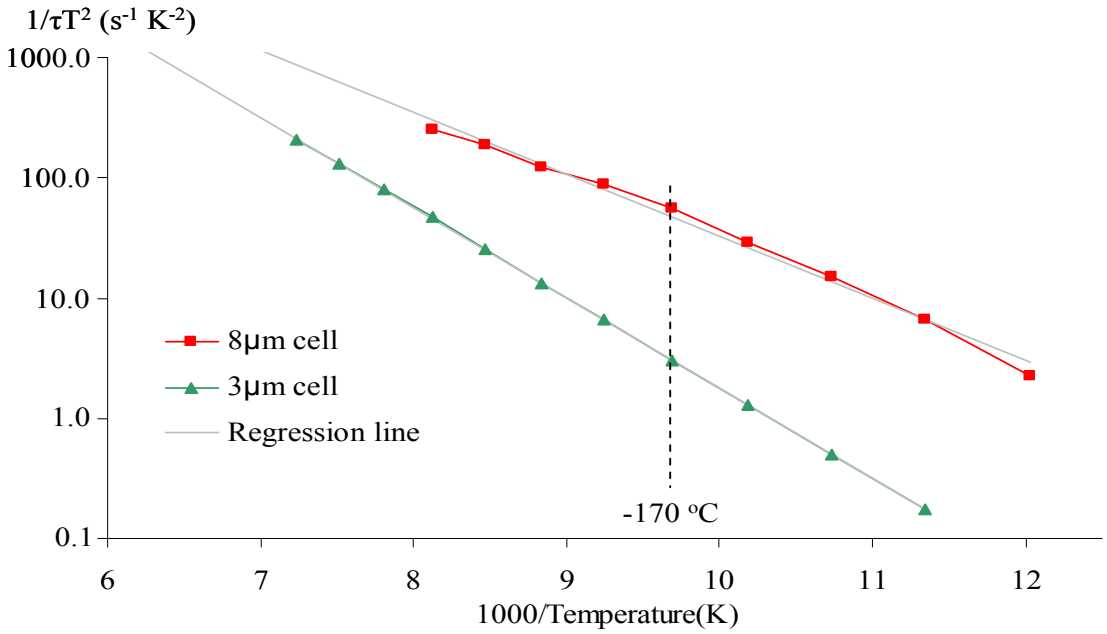

Figure 2.8 Arrhenius plot with regression lines for SCAPS simulated 8μm and 3μm cells.

In summary, this simulation model offers a plausible explanation for a number of observed phenomena with experimental data collected from thin film CdTe solar cells with high concentrations of DES. These include:

- Loss of AS signal for shallow DES when the CdTe layer is thin
- Distortions to the measured values for E_a and σ_a due to Fermi level pinning and the fact that ω_t is a function of both E_t and E_f.
- Stretched exponential behavior when there is only a single discrete DES energy level.

3. CELL PRODUCTION AND STANDARD TESTING PROCEDURES

To date all high performance CdTe solar cells have included Cu and $CdCl_2$ in post-deposition heat treatments [9]. While the complex interaction between these two additives is known to favorably change the defect structures and electronic properties that control performance, the understanding of this process remains incomplete. Therefore, this study has applied admittance spectroscopy (AS), capacitance transient (CTr), and standard solar cell analysis techniques to examine differences in deep electronic states (DES) for CdTe cells produced with and without both Cu and $CdCl_2$. In addition, this study examines changes in DES with stressing. This section is divided into two subsections. The first one describes the production process for the cells used in the study. The second describes the standard testing procedures.

3.1 Production Processes for CdTe Solar Cells Used in Experiments

The 2x2 matrix of Cu/no Cu and $CdCl_2$/no $CdCl_2$ cells with replicates were obtained from four sources: Dave Albin at the National Renewable Energy Laboratory (NREL) Brian McCandless at the Institute for Energy Conversion (IEC), Xuanzhi Wu (NREL), and Alan Enzenroth at Colorado State University (CSU).

3.1.1 Cells produced by D. Albin at NREL.

The cells were grown on a single Corning 7059 glass substrate with a SnO_2 bi-layer (500 nm F-doped/ 100 nm undoped) as the front transparent contact. The CdS window layer was deposited by chemical bath deposition (CBD) to a thickness of ~80nm followed by close-spaced sublimation (CSS) of the CdTe absorber layer to a thickness of ~8μm. The substrate was then quartered and the two $CdCl_2$-treated devices were annealed at 400^{o}C in a CSS-arrangement using anhydrous $CdCl_2$ as a source in an ambient of 100 torr Oxygen/400 torr Helium for 7 min. All devices were then etched with a nitric-phosphoric acid (NP) etch. Back contact carbon-based paste (Electrodag 114) was applied to the CdTe surface by brushing. The two devices with Cu had $Cu_{1.4}Te$ powder added to the paste.

The back contact areas are approximately 0.5cm^2 and a 260^{o}C anneal in helium was applied to activate the contact. To avoid back to front contact electrical shorting, a ~1 mm lateral margin of solar cell material was retained around the back contact. This enhances current collection at the

back contact edges yielding higher short-circuit current values than would be obtained without the margin. Two cells were produced for each Cu and $CdCl_2$ category for a total of eight cells.

3.1.2 Cells produced at IEC.

The cells supplied by B. McCandless were grown on TEC15 glass TCO with a Ga coating oxidized at 500^{o}C to serve as the bi-layer. The CdS window layer was grown by chemical surface deposition where a solution at ambient temperature is applied to a pre-heated glass/TCO substrate producing a film with low particulate density. Then a $CdCl_2$ vapor treatment is applied. The CdTe absorber layer was deposited by vapor transport at 550^{o}C on a moving substrate at a 2.5 cm/min translation speed, giving a 10 μm/min equivalent growth rate. The cells with $CdCl_2$ were exposed to $CdCl_2$ vapor at 415^{o}C for 25 minutes in an argon and oxygen atmosphere. Then all cells were sequentially etched in bromine-methanol, dichromate, and hydrazine. The cells with Cu had 15nm of Cu deposited by evaporation and all cells had 50 nm of Ni deposited by evaporation.

Each back contact area is 0.36cm^2 and a 25 minute anneal at 180^{o}C in Argon was applied. The cell edge was scribed down to the front contact and an Indium solder strip was applied followed by a dip in a weak bromine methanol solution. Four replicates were produced for each category for a total of 16 cells.

3.1.3 Cells produced by X. Wu at NREL

The description of processing performance and some properties of the high-efficiency CdTe cells produced by Dr Wu can be found in Ref. [17]. We are not well aware of all the details of processing six cells we received from Dr. Wu for studies except those mentioned in Sec. 4.3.

3.2 Standard Testing Procedures

Upon receipt, all cells were subjected to the standard room temperature J-V analysis which is a fairly rapid procedure. Then, based on J-V results, cells were selected for QE testing and the full suite of temperature controlled testing including J-V-T, C-V-T, AS, and CTr.

3.2.1 J-V and J-V-T tests

After a dark J-V curve was taken, the light source was turned on and allowed to settle for 5 seconds, and then a light J-V curve was taken. For the standard room temperature J-V measurements, the light source consists of five halogen light bulbs housed in a home built 70x70x90cm box. The color spectrum of our light source is cooler than the standard sun with more intensity in the red and less in the blue. The measured efficiency values have typically been about *one percent absolute lower* than the official NREL determinations.

For the temperature controlled current voltage (J-V-T) measurements, the insulated copper chamber and optical fiber cable light source were used. The light intensity of one sun is approximate and it is suspected to be non-uniform over the area of the cell. However, for each test sequence where the cell is left in place, the light intensity is reproducible. This is adequate since the goal is to compare J-V curves at different temperatures from a single run. The J-V-T measurements are taken while the chamber and cell are being cooled for a subsequent C-V-T set of measurements. During this time the Keithley source meter is connected to the chamber in place of the LCR meter. The first measurement is taken when the chamber reaches 20^{o}C and then at 10^{o}C intervals down to near liquid nitrogen at -190^{o}C. For comparisons between runs, a calibration factor is used that is the ratio of the J_{SC} value on the standard J-V system to the J_{SC} value at a nominal 20^{o}C.

3.2.2 Quantum efficiency

The CSM QE system consists of a sample stage with a pinhole to admit the single wavelength light, a monochromater to supply the single wavelength light, a chopper and lock-in amplifier to augment the resulting current signal, and a Keithley source meter to apply bias. No white light bias is applied as it overloads the current amplifier.

3.2.3 Capacitance-voltage profiling at varying temperature (C-V-T)

The thermally controlled C-V-T measurements apply a 10mV AC signal at 100kHz to obtain the admittance measurements. The LCR meter applies a bias sweep starting at -2V and incrementing in 50mV steps to +0.5V. An admittance measurement is recorded at each step. To check for hysteresis a reverse sweep immediately follows starting at +0.5V and decrementing in

50mV steps down to -2V. The C-V measurements are taken in the dark at 10°C intervals starting at -190°C and going to 20°C. The apparatus setup is described in our Final 2005 Report to NREL [1] and in [8]

3.2.4 Admittance spectroscopy (AS)

The AS measurements applied a 10 mV AC signal with a frequency sweep starting at 25 Hz and incrementing by 12 steps per decade up to 1 MHz. The signal was often noisy below 1 kHz and below 250Hz it was so noisy that it was of no practical use, even with the doubly insulated BNC cables and the grounded copper chamber. An isolating power supply did not reduce the noise. The maximum frequency for the HP4284A LCR meter is 1MHz. No bias was applied during these measurements.

3.2.5 Capacitance transients (CTr)

The CTr measurements consist of a timed interval sequence of admittance readings taken with a 10mV, 100kHz AC signal. The bias sequence started with 30s at 0V to establish a baseline, followed by a 300s filling pulse at +0.5V, and ended with a 300s 0V recovery period.
A logarithmically increasing time interval between measurements was used. This did not cause any loss of information as the transients have an exponential (or close to that) time dependency. An advantage of the logarithmic time interval is reduced noise in the $\frac{dC(t)}{d\ln(t)}$ versus $\ln(t)$ graph. With a fixed time measurement interval, the noise occurs near the end of the 300 s period where the $\Delta\ln(t)$ in the denominator becomes very small and amplifies any $\Delta C(t)$ signal noise in the numerator.

3.2.6 Temperature

The AS and CTr measurements are taken in sequence at preset temperatures ranging from 85°C to -190°C. The AS measurements are taken before the CTr measurements to minimize any residual transient contamination. This works under the assumption that the time between the measurements at subsequent temperatures is sufficient so that any residual transient from the CTr reading is negligible.

The standard procedure is to heat the system first and allow it to gradually cool to room temperature. Soon afterwards the sample is cooled by liquid nitrogen and then allowed to gradually warm to room temperature. This has resulted in the best data stitching between the heating and cooling cycles. Room temperature capacitances changed by as much as 10% following a heating cycle. We suspect that this is caused by metastable states set at the modestly elevated temperature of 85^{o}C. If the cell remains at room temperature for a few days the measured capacitances return to their original value. However, if the cell is immediately cooled, the metastable state is frozen-in and remains for the duration of the cooling cycle resulting in better data stitching across room temperature.

The preset test trigger temperature intervals range between 4^{o}C and 10^{o}C. The tighter intervals are used in temperature ranges where signatures of interest are often found.

4. RESULTS AND DISCUSSION

Results of experiments conducted on completed CdTe solar research cells obtained from four different sources, are discussed in this section. Four post-deposition treatment categories from each source were studied:

(1) Cells with yes-Cu/yes-$CdCl_2$ treatment.

(2) Cells with no-Cu/yes-$CdCl_2$ treatment.

(3) Cells with yes-Cu/no-$CdCl_2$ treatment.

(4) Cells with no-Cu/no-$CdCl_2$ treatment.

These cells were tested with J-V, QE, C-V, J-V-T, AS, and CTr.

The results and discussion for the cells from different sources are presented in the following sections: 4.3.1- D. Albin's cells; 4.3.3 – IEC cells; 4.3.3 - Wu's cells; 4.3.4 – Enzenroth's cells.

4.1 NREL (D. Albin) Cells.

The CdTe solar cells obtained from Dave Albin at NREL yielded the cleanest results and were the easiest to interpret. Experimental data was collected from both replicate cells from each of the four categories. However, differences between cells within each category were negligible and only the first cell results from each category are reported.

4.1.1 J-V, QE, C-V results.

Results of J-V measurements under illumination for each cell category are tabulated in table 4.1. As expected, the yes-Cu/yes-$CdCl_2$ cell had the highest efficiency η and the no-Cu/no-$CdCl_2$ cell had the lowest η. Adding either the Cu or the $CdCl_2$ treatment improved all of the performance metrics with one significant exception. The Cu treatment decreased the short circuit dynamic resistance R_{SC} ("shunt resistance") and for the yes-$CdCl_2$ cell it lowered the J_{SC} as well. The J-V curves are shown in figure 4.1 and the rollover effect is evident for the no-Cu cells as a result of the back contact Schottky barrier.

Table 4.1 Performance parameters for Albin's cells with yes/no Cu and yes/no $CdCl_2$.

Cu/ $CdCl_2$	η %	V_{OC} V	J_{SC} $mA\ cm^{-2}$	FF %	R_{SC} Ωcm^2	R_{OC} Ωcm^2
yes/yes	12.4	0.82	23.9	63	578	5.2
no/yes	11.1	0.78	24.2	59	1350	11.2
yes/no	9.0	0.72	22.0	57	276	6.3
no/no	7.3	0.69	21.2	50	287	10.5

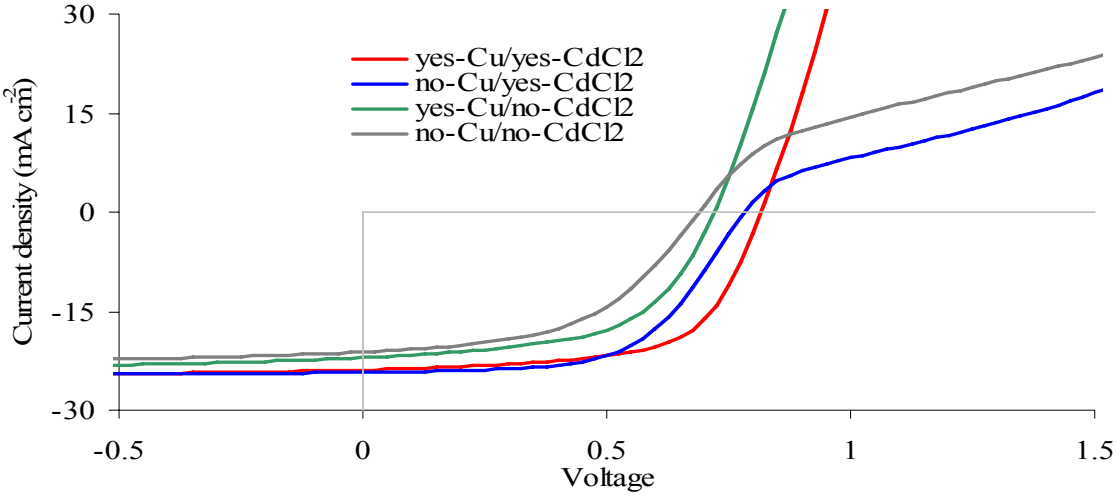

Figure 4.1 J-V curves for NREL cells with yes/no Cu and yes/no $CdCl_2$ treatments.

The quantum QE results are shown in figure 4.2.

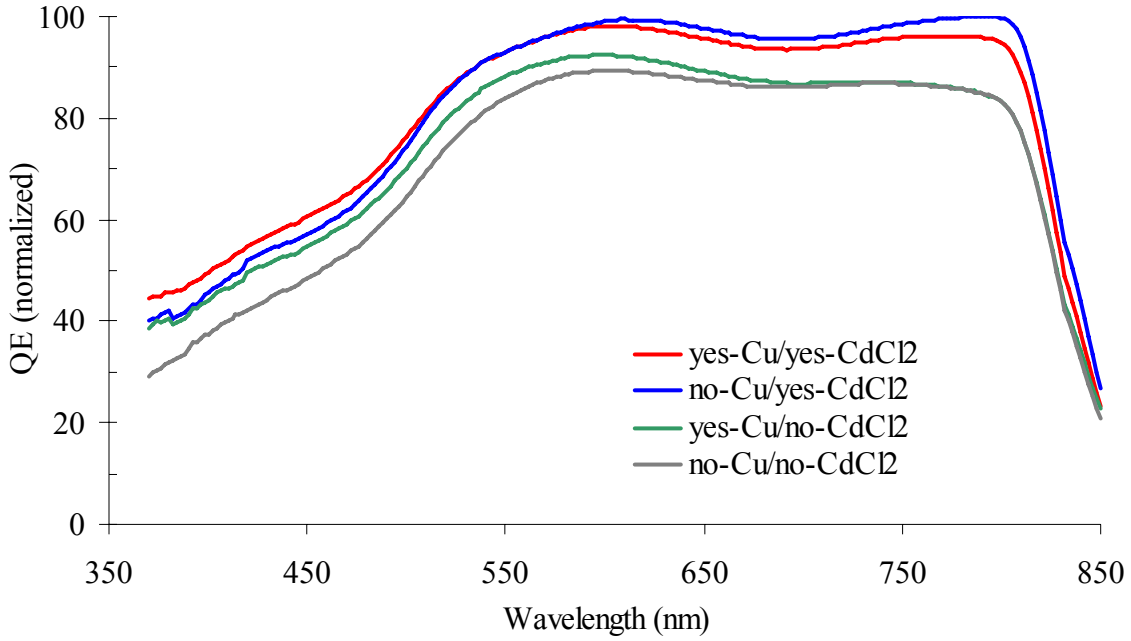

Figure 4.2 QE curves for NREL cells with yes/no Cu and yes/no $CdCl_2$ treatments.

The yes-$CdCl_2$/no-Cu treatment enhanced overall current collection indicating improvement of carrier transport both in CdTe and CdS. The yes-Cu/no-$CdCl_2$ treatment enhanced QE mostly in he short λ range. Adding the Cu treatment to the yes-$CdCl_2$ cell decreased the long λ QE indicating that Cu attenuated the $CdCl_2$ improvement to the carrier transport further from the junction. However, QE at the photon energy above the CdS bandgap is higher than for $CdCl_2$ only. Based only on these data it is difficult to propose unambiguous explanations for the observed effects of Cu.

C-V profiles taken at room temperature are shown in figure 4.3. The reverse bias voltage range is not sufficient at room temperature to reach the full depletion of the CdTe layer ~8 μm thick.

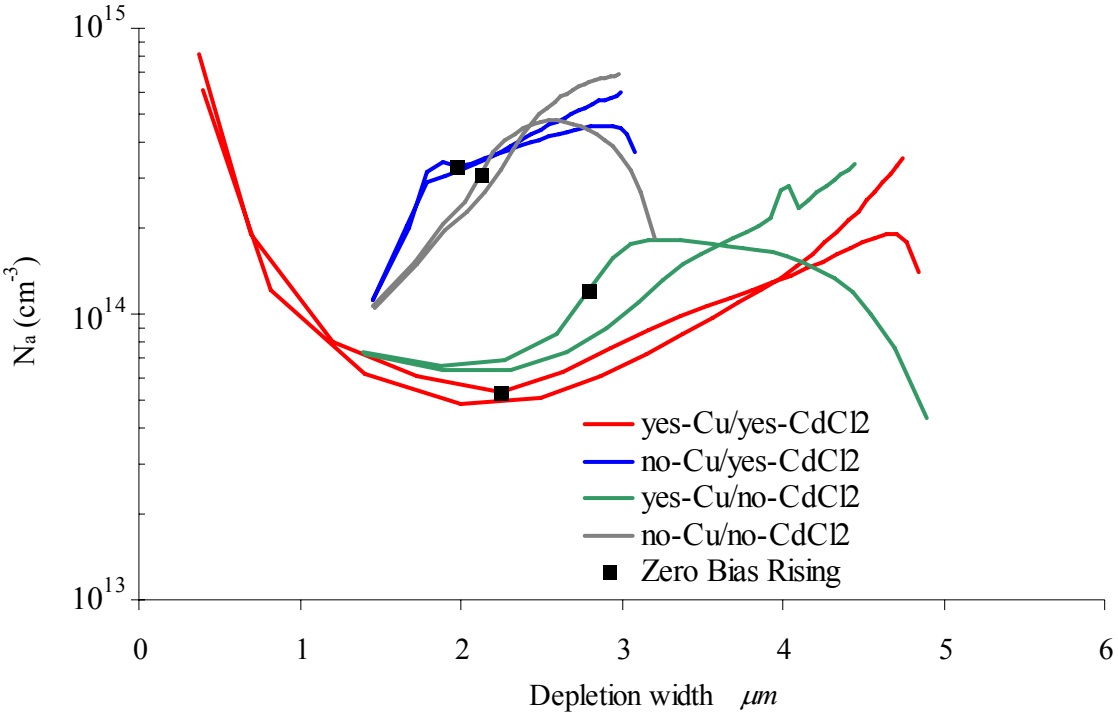

Figure 4.3 Room temperature C-V profiles for NREL (Albin's)cells.

The yes-Cu cells had a lower apparent doping level than both $CdCl_2$-treated and untreated cells. This looks surprising since introducing Cu is supposed to act as an acceptor doping. There is a possibility to explain this effect by pinning the Fermi level by partially compensated deep acceptor states provided by Cu_{Cd} defects. In Sec.2, SCAPS SIMULATION, a similar effect was demonstrated for shallower DES at lower temperatures.

Hysteresis can be seen for the -2V to +0.5V to -2V bias voltage loop in the C-V profile for all of the cells (differences in N_a on the left side of graph) and this is due to slow CTr's as was discussed in section 1. This hysteresis is less pronounced for the yes-$CdCl_2$ cells indicating that the $CdCl_2$ treatment alters these DES. Possibly these changes reduce SRH recombination resulting in the improved current collection as seen in the QE measurements and J_{SC} values.

4.1.2 J-V-T Results

Figure 4.4 shows J-V curves for the yes-Cu/yes-$CdCl_2$ cell for temperatures ranging from 20°C to -180°C in 10°C intervals. As the cell initially cools (blue curves), the increasing Schottky barrier rollover effect can be seen due to the exponential decrease with temperature of the reverse

saturation current. As the cell continues to cool (green) the Schottky barrier increases further. As the cell cools further (red) J_{SC} decreases rapidly indicating that the free carriers are "freezing out" and that the cell is losing its ability to collect the photocurrent. The other three cells have the same general J-V-T structure.

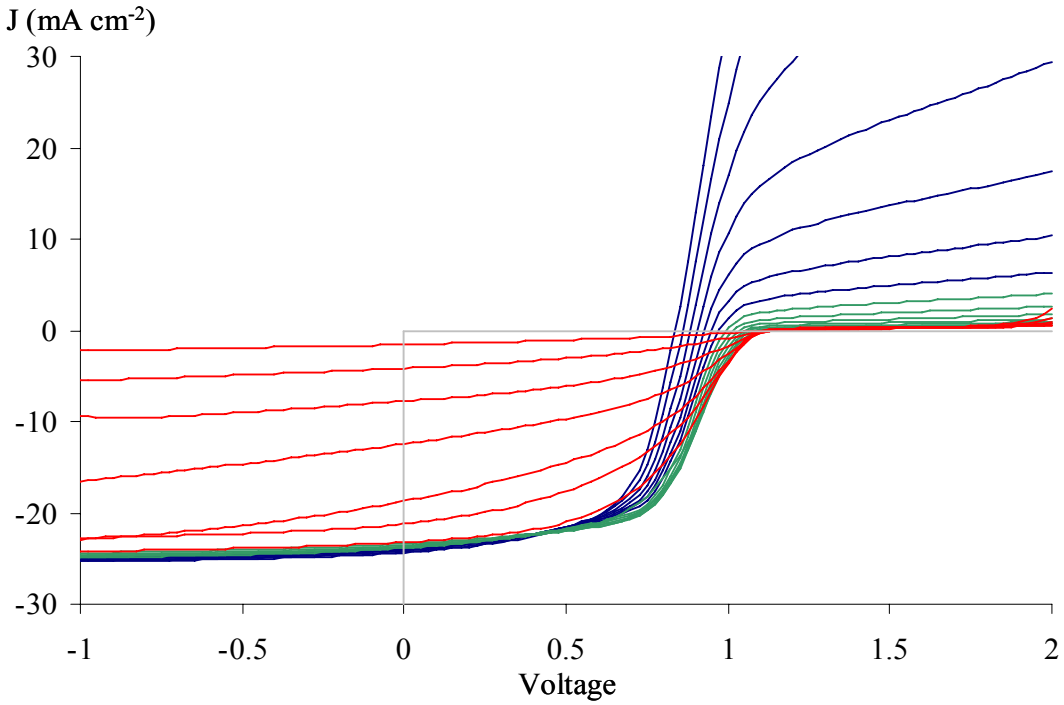

Figure 4.4 J-V-T curves for cell with the yes-Cu/yes-$CdCl_2$ treatment at 10° C increments ranging from 20°C to -40°C (blue), -50°C to -110°C (green), and -120°C to -180°C (red).

The subtle differences are better highlighted by graphing V_{OC} and J_{SC} versus T as is shown for the four cells in figure 4.5.

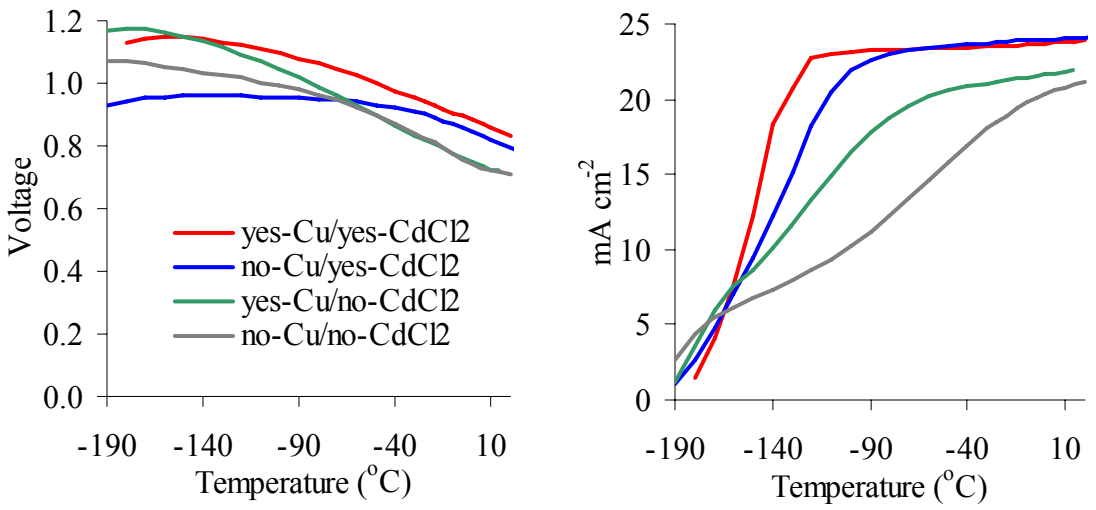

Figure 4.5 V_{OC} and J_{SC} versus T graphs for cells with yes/no Cu and yes/no $CdCl_2$ treatments.

At room temperature the highest V_{OC} value is demonstrated by the yes-$CdCl_2$ cells, almost the same for yes- and no-Cu. The no-$CdCl_2$ cells have the V_{OC} values equal to each other and lower by ~ 100mV than the former two cells. At T= -190^{0}C both yes-Cu cells have higher V_{OC} than no-Cu cells: ~1180 mV and ~ 1150 mV respectively for no-Cl and yes-Cl cells. The lowest $V_{OC} \sim 930\,mV$ has the yes-Cu/no-$CdCl_2$ cell.

J_{SC} decreases modestly as T starts to decrease from room temperature and this may be attributed to narrowing absorbed solar spectrum caused by an increasing band gap. For CdTe, $dE_g/dT = -1.7 meV/^o K$ [9].

For the yes-$CdCl_2$ cells, the carrier freeze out begins abruptly at lower T. It could be explained by freezing out the acceptor state that dominates the free carrier concentration in this temperature range. It happens when T becomes sufficiently low so that $(E_t - E_F)/kT >> 1$, which eliminates the DES ionization and its contribution to the carrier transport. An approximate estimate of this acceptor energy level can be made by equating it to the Fermi level at the temperature where J_{SC} begins to drop and by neglecting the influence of light on the majority carrier holes concentration. The results of such estimates based on figure 4.5 data are presented in Table 4.2.

Table 4.2 Estimate of the DES energy level based on J_{SC} freeze out temperature for Albin's cells with yes/no Cu and yes-$CdCl_2$ treatments.

$Cu/CdCl_2$	N_{C-V} at room T (cm^{-3})	Freeze out temperature (^oC)	DES level estimated from Fermi level (eV)
yes/yes	$5x10^{13}$	-120	0.16
no/yes	$3x10^{14}$	-90	0.16

The energy level of 0.16eV is close to that reported for the chlorine A-center $V_{Cd}^{2-} - Cl_{Te}^{+}$ [10,11], suggesting that it dominates the enhanced current collection in the yes-$CdCl_2$ cells. This contrasts with the no-$CdCl_2$ cells where there is no pronounced T -demarcation for the beginning of carrier freeze-out suggesting that current collection is enabled by DES with a range of defect energy levels.

The graph of R_{OC} versus T in figure 4.6 shows the "series resistance" thermal dependencies for the differently processed cells.

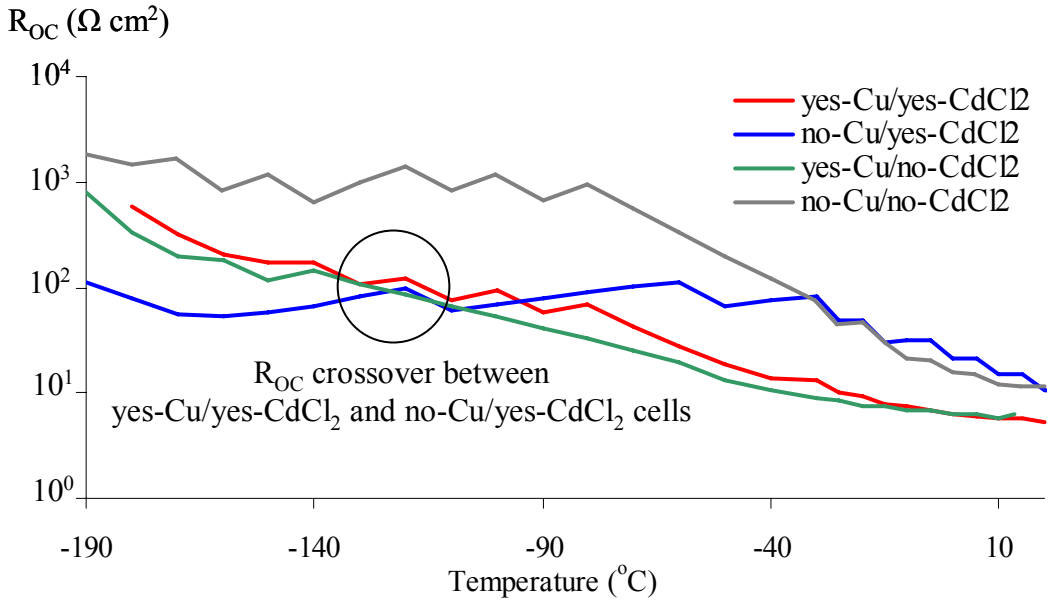

Figure 4.6 R_{OC} versus T graphs for NREL cells with yes/no Cu and yes/no $CdCl_2$ treatments.

The yes-Cu cells start off with the lowest resistances of about 5 Ω cm^2 at 20^{o}C and steadily increase to about 1000 Ω cm^2 at -190^{o}C. The no-Cu/no-$CdCl_2$ cell starts off with 10 Ω cm^2 at 20^{o}C and climbs to about 1000 Ω cm^2 at -80^{o}C where it stays fairly constant to -190^{o}C. The no-Cu/yes-$CdCl_2$ cell starts off with 10 Ω cm^2 at 20^{o}C and climbs to about 100 Ω cm^2 at -30^{o}C where it stays fairly constant to -190^{o}C. This sets up a series resistance crossover point between the yes-Cu and no-Cu/yes-$CdCl_2$ cells at about -100^{o}C. The explanation relies on a combination of better transport properties from Cu_{Cd}, depletion of V_{Cd} by Cu_{Cd}, and freeze out of Cu_{Cd} around 100 K as discussed later.

4.1.3 AS Results

Figure 4.7 shows $C_p(T)$ dependence in separate graphs for each of four (yes/no- $CdCl_2$, yes/no-Cu) cells .

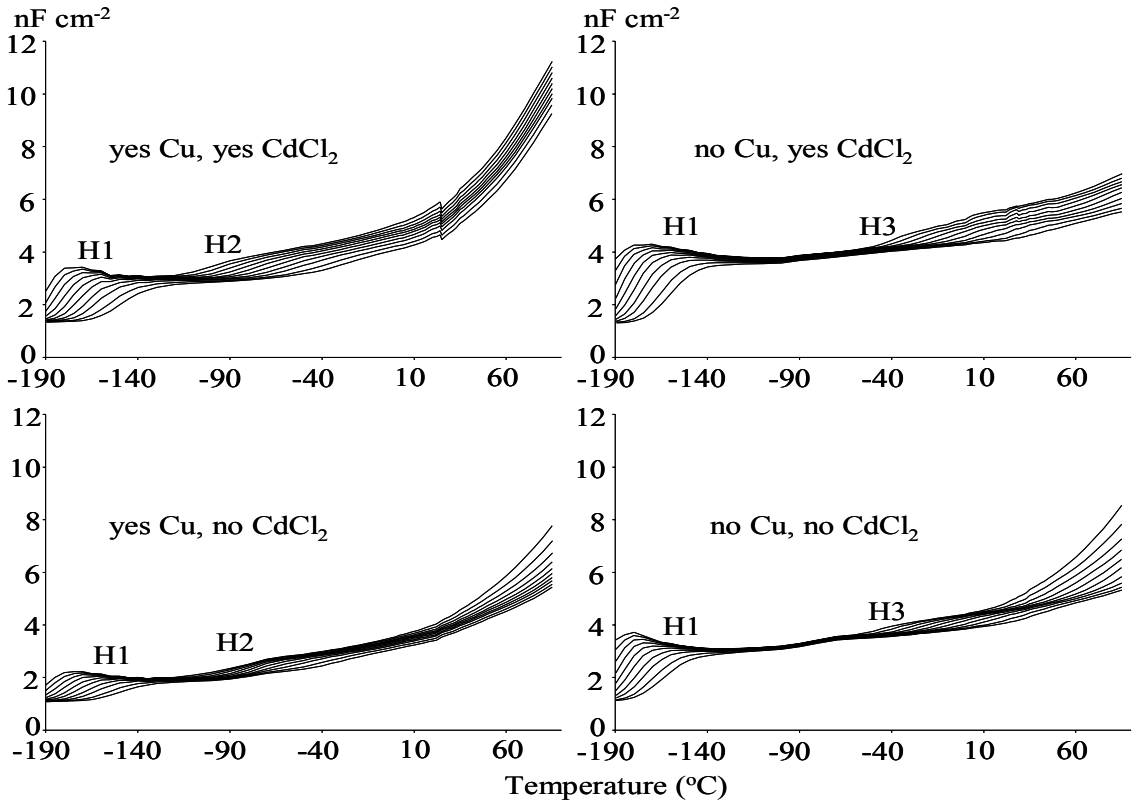

Figure 4.7 AS graphs of C_p versus T for NREL cells with yes/no Cu and yes/no $CdCl_2$ treatments. Three detected DES signatures are labeled H1, H2, and H3.

Three distinct majority carrier or hole trap signatures were identified and analyzed. They were grouped by a combination of their activation energy, E_a, and their detection temperature range. Differences were observed between each of the four differently processed cells and the most noticeable were between the yes-Cu and no-Cu cells. As explained in Section 1 each line corresponds to a fixed AC signal frequency ranging from 1 kHz (top line) to 1 MHz (bottom line). The analysis results are summarized in table 4.3.

Table 4.3 Summary of detected AS signatures H1 through H3 for NREL cells with yes/no Cu and yes/no $CdCl_2$ treatments. The E_a estimates include a 75% linear regression confidence interval (experimental uncertainty not included).

Trap	Cu/$CdCl_2$	E_a eV	σ_a cm^2	C_t^0 $nF\ cm^{-2}$	β	Temp K
H1	yes/yes	.133±.003	$4x10^{-14}$	2.1	0.50	83 to 118
	no/yes	.128±.002	$8x10^{-14}$	3.0	0.48	83 to 108
	yes/no	.128±.003	$2x10^{-14}$	1.1	0.50	83 to 118
	no/no	.145±.003	$1x10^{-12}$	2.5	0.43	83 to 108
H2	yes/yes	.305±.005	$9x10^{-14}$	0.9	0.49	183 to 238
	yes/no	.292±.005	$6x10^{-14}$	0.5	0.54	173 to 233
H3	no/yes	.475±.003	$7x10^{-13}$	0.6	0.78	243 to 310
	no/no	.464±.005	$8x10^{-13}$	0.5	0.68	238 to 300

A strong H1 signature was observed in all four cells with $E_a \sim 0.13eV$. This is consistent with reported E_a values for the singly ionized cadmium vacancy V_{Cd}^- [10] as well as the acceptor A center $V_{Cd}^{2-} - Cl_{Te}^+$ acceptor [10, 11]. The NP etch leaves behind a ~0.1μm thick free Te layer at the back surface and a Te enriched CdTe underneath [12] which serves as a source of V_{Cd}^- as well as tellurium interstitials Te_i^- that can diffuse into the CdTe. The C_p value at fixed frequencies decreases with increasing temperature indicating a steep concentration gradient near the back contact as shown by the SCAPS simulation in Section 2. Also, the C_t^0 values indicate that the concentration of H1 *decreased* with the addition of Cu which is consistent with Cu substitutions on cadmium vacancies Cu_{Cd}^- that is replacement of shallower acceptor V_{Cd}^- by the deeper one Cu_{Cd}^-. This is also consistent with the previous observations of the temperature influence on the electroluminescence pattern in the cells with the intentional lateral nonuniformity of Cu-doping

[16]. The concentration of H1 *increased* with the addition of $CdCl_2$ which is consistent with the formation of $V_{Cd}^{2-} - Cl_{Te}^{+}$. Thus, the H1 signature has been attributed to a combination of V_{Cd}^{-} and A center $V_{Cd}^{2-} - Cl_{Te}^{+}$.

The H2 signature was only detected in cells that had the Cu treatment. The $E_a \approx 0.3eV$ is close to the values previously attributed to Cu_{Cd}^{-} [13, 14]. We also assign this signature to the same defect. The H2 concentration was higher with $CdCl_2$ implying that the defects induced by $CdCl_2$ (probably Cl-induced donor) increased the solubility of Cu_{Cd}^{-} (well known effect of the Fermi level influence on the solubility of charged defects, see, e.g., [15]) .

The H3 signature with an E_a of 0.47 eV was only detected in cells with no intentionally added Cu. It is possible that H3 is caused by the negative U-center Te_i^{2-}. As mentioned above the NP etch can increase the tellurium interstitials. The apparent discrepancy between the measured $E_a \approx 0.47eV$ and the calculated transition (0/-2) energy of 0.57 eV [15] can be eliminated by suggesting the negative U-nergy value of –0.1eV. However, we remain cautious about assigning H3 to a specific defect. The H3 β values were higher (0.68 and 0.78), possibly indicating less Fermi level pinning for this defect (see results of simulation in Section 2).

At warmer temperatures (30°C and above), the yes-$CdCl_2$ cells show a fairly constant spread in C_p values with frequency indicating a continuous band of energy levels possibly due to interfacial or GB surface DES. The no-$CdCl_2$ cells show a growing magnitude with temperature possibly indicating a large magnitude defect beyond the measurement temperature range.

4.1.4 CTr Results

Two minority carrier traps labeled E2, E3 and two majority carrier traps labeled H4, H5 were detected using CTr; the results are tabulated in table 4.4. The most striking trap H5 was detected in the yes-Cu/yes-$CdCl_2$ cell. It has a large density ($C_t^0 = 40nF\ cm^{-2}$), a high activation energy, $E_a = 0.83eV$ (deep state), and a small apparent capture cross section $\sigma_a = 8x10^{-17}\,cm^2$.

Data from the other cells suggest that they also possess a high magnitude transient that would be detected with higher temperature testing. This can be seen in figure 4.8 that shows the temperature dependent amplitude ΔC of CTr caused by the forward bias (FB) charging pulse for the four cells. With the graph scale set to show H5, the other DES E2, E3, H4 are barely visible.

There is insufficient information to reliably assign these signatures to specific defects. E2 with $E_a = 0.21eV$ is possibly a Cu_i^{2+} donor and E3 with $E_a = 0.43eV$ is possibly a Cl_{Te}^{+} donor [15].

Table 4.4 Summary of detected CTr minority carrier (E2, E3), and majority carrier (H4, H5) trap signatures for NREL cells. The applied bias listed indicates whether the CTr was detected during the charging pulse or during the subsequent recovery period.

Trap	$Cu/CdCl_2$	E_a eV	σ_a cm^2	C_t^0 $nF\ cm^{-2}$	β	Applied Bias V	Temp K
E2	yes/yes	.214±.030	$1x10^{-17}$	0.6	0.70	+0.5 Pulse	103 to 123
E3	no/yes	.427±.019	$2x10^{-14}$	0.2	1.20	+0.5 Pulse	153 to 173
H4	no/yes	.524±.020	$4x10^{-15}$	0.2	0.87	0 Recovery	193 to 213
	yes/no	.688±.017	$9x10^{-12}$	0.5	0.46	0 Recovery	203 to 223
	no/no	.563±.011	$3x10^{-14}$	0.2	0.77	0 Recovery	193 to 213
H5	yes/yes	.826±.017	$8x10^{-17}$	40.0	0.52	+0.5 Pulse	328 to 358

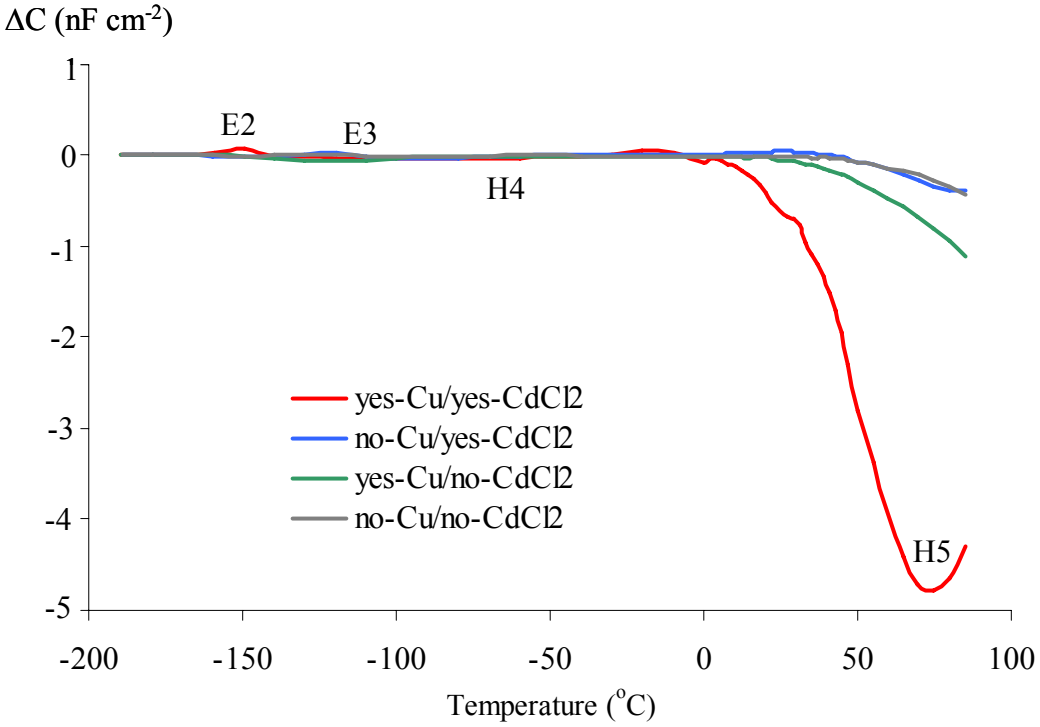

Figure 4.8 The amplitude ΔC of capacitance transient caused by the FB charging pulse for NREL cells with yes/no Cu and yes/no $CdCl_2$ treatments. Temperature dependence

Figure 4.9 shows the Arrhenius plot for both the AS and CTr detected traps. The AS detected traps H1, H2, H3 with τ ranging from microseconds to milliseconds can be seen in the upper portion of the graph and the CTr detected traps E2, E3, H4, H5 with τ ranging from seconds to 10^3s can be seen in the lower portion of the graph. This shows how the CTr in this study explores a new region in the Arrhenius space. The unique experimental apparatus and custom software expressly designed and built for this purpose have facilitated this.

There is greater uncertainty in the CTr E_a estimates as indicated by the 75% confidence intervals. This is caused in part by the narrow 1000/T range.

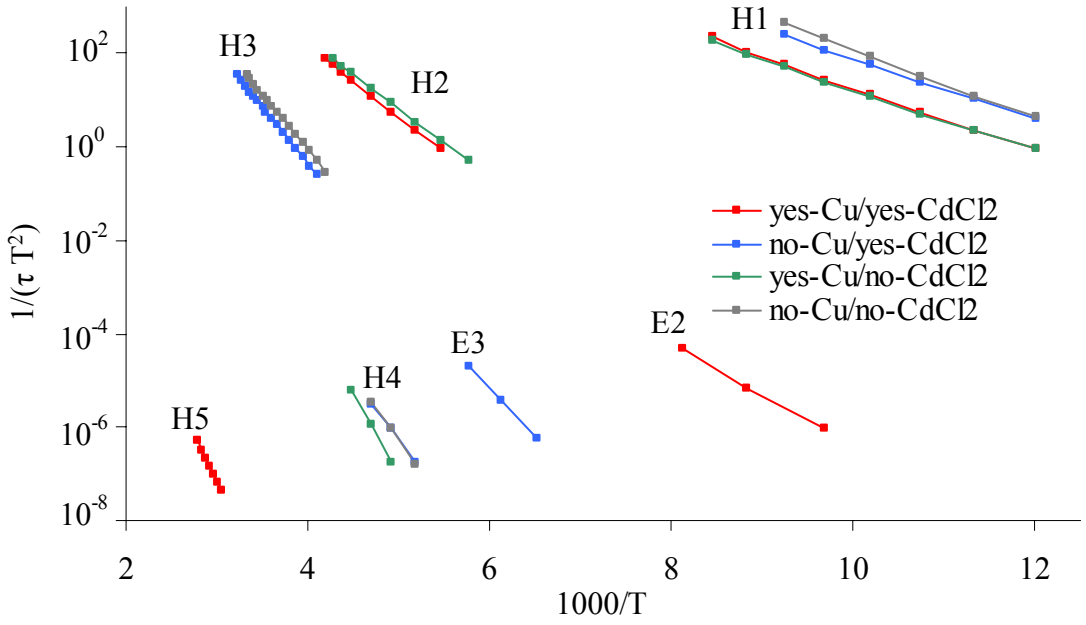

Figure 4.9 Arrhenius plot for NREL cells with yes/no Cu and yes/no $CdCl_2$ treatments. H1, H2, H3 were detected with AS, and E2, E3, H4, H5 were detected with CTr.

4.2 IEC Cells

Room temperature J-V analysis was performed on the four replicates from each of the four categories on the cells obtained from Brian McCandless at the Institute for Energy Conversion (IEC) in Delaware. A number of the cells had fairly severe shunting indicating that they had "shorted out". For each category, the cell with the best performance was selected for the full suite of QE, C-V, J-V-T, AS and CTr testing.

4.2.1 J-V, QE, C-V Results

Performance results from each cell category for J-V measurements under illumination are tabulated in table 4.5. The performance order relation was the same as for the NREL cells with the exception of the yes-Cu/yes-$CdCl_2$ cell which had lower η, V_{OC}, FF and R_{SC} probably caused by shunting. The poor η for the no-$CdCl_2$ cells are largely due to low J_{SC} indicating poor photocurrent collection.

Table 4.5 J-V performance results for IEC cells with yes/no Cu and yes/no $CdCl_2$.

Cu/ $CdCl_2$	η %	V_{OC} V	J_{SC} $mA\ cm^{-2}$	FF %	R_{SC} Ωcm^2	R_{OC} Ωcm^2
yes/yes	6.7	0.66	23.3	44	197	9.2
no/yes	9.2	0.70	23.6	55	579	9.0
yes/no	3.4	0.59	12.0	48	330	14.4
no/no	3.0	0.59	11.5	44	309	24.1

The J-V curves are shown in figure 4.10. Similar to the NREL cells, the rollover effect resulting from the back contact Schottky barrier is evident in the no-Cu cells.

The QE curves, calibrated to the J-V measurement J_{SC} values are shown in figure 4.11. The largest contrast is with the overall collection between the yes- and no-$CdCl_2$ cells. The yes-$CdCl_2$ cells had higher QE values for the shorter wavelength, indicating better photocurrent collection near the junction.

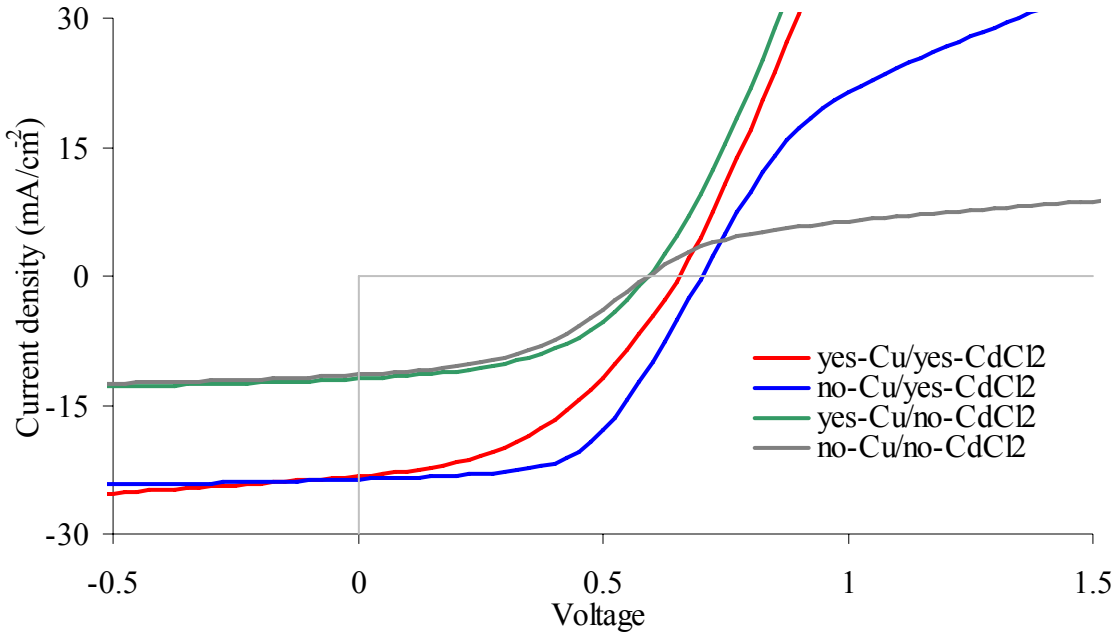

Figure 4.10 J-V curves for IEC cells with yes/no Cu and yes/no $CdCl_2$.

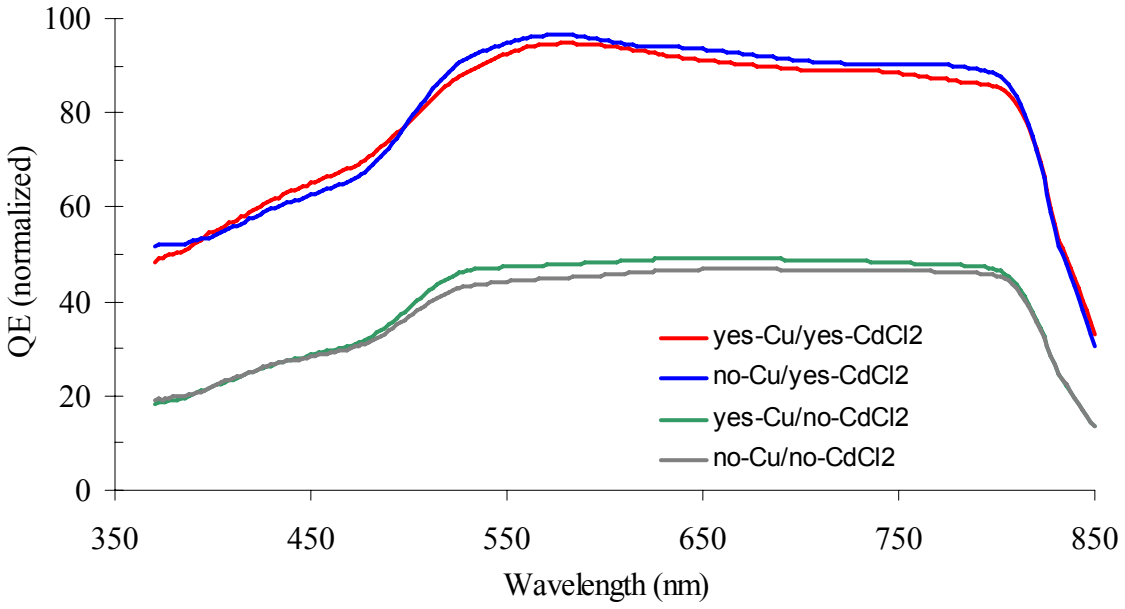

Figure 4.11 QE curves for IEC cells with yes/no Cu and yes/no $CdCl_2$.

C-V profiles taken at room temperature are shown in figure 4.12. The yes-$CdCl_2$ cells have a narrower depletion width indicating a higher space charge density (SCD) near the junction. This

implies a stronger electric field, which improves the electron/hole separation. With most of the light being absorbed within the first two μm this can explain why the yes-$CdCl_2$ cells have better current collection. The depletion regions of the IEC no-$CdCl_2$ cells are wider (>4μm at zero bias) than any of the NREL cells implying that they have the weakest electric field. This is consistent with the flat low QE curves indicating weak photocurrent collection throughout the $h\nu \le E_g^{CdTe}$ photon energy range. For the IEC cells the $CdCl_2$ treatment increases the apparent doping concentration, which contrasts with the NREL cells where it is the Cu treatment that had this effect.

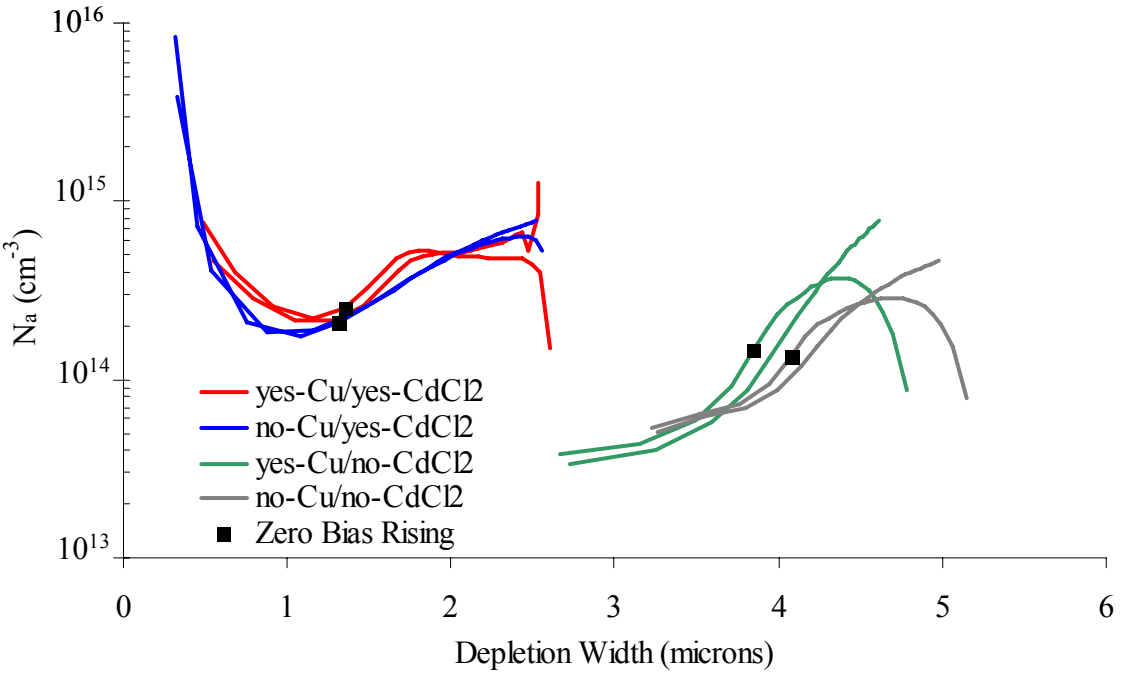

Figure 4.12 Room temperature C-V profiles for IEC cells with yes/no Cu and yes/no $CdCl_2$.

Figure 4.13 graphs V_{OC} and J_{SC} versus T for the four differently processed cells. For the yes-$CdCl_2$ cells, carrier freeze-out begins at about -120°C. With a C-V profile apparent doping level $N_a \approx 2x10^{14}$, the activation energy for the doping defect is approximately $0.14eV$ which is close to that derived for yes-$CdCl_2$ NREL cells. This is a further indication that the A-center $V_{Cd}^{2-} - Cl_{Te}^{+}$ is largely responsible for the superior current collection in the yes-$CdCl_2$ cells.

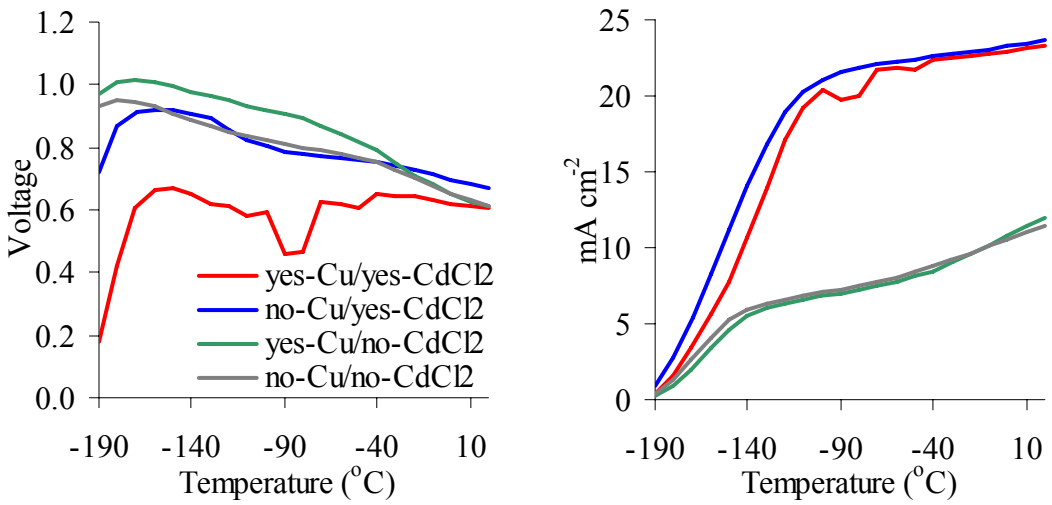

Figure 4.13 V_{OC} and J_{SC} versus T for IEC cells with yes/no Cu and yes/no $CdCl_2$.

4.2.2 AS and CTr Results

Similarly to the NREL cells, AS has detected three distinct majority carrier traps, H1, H2, and H3. Capacitance transient measurements have detected two slow traps: labeled H5 for holes and E3 for electrons. The trap signatures are presented in table 4. The $C_p(f,T)$ dependencies are shown in figure 4.14, the Arrhenius plots for both the AS and CTr detected traps - in figure 4.15.

Table 4.6 The DES signatures detected by AS (H1 through H3) and CTr (E3, H5)

Trap	Cu/$CdCl_2$	E_a eV	σ_a cm^2	C_t^o nF/cm^2	β	Applied Bias, V	Temp °K
H1	yes/yes no/yes	.160ϒ.004 .157ϒ.008	$5x10^{-13}$ $8x10^{-13}$	1.1 3.1	0.46 0.38	-	88 to 118 83 to 113
H2	yes/yes yes/no	.358ϒ.011 .353ϒ.016	$2x10^{-13}$ $1x10^{-13}$	2.6 0.6	0.60 0.37	-	193 to 248 203 to 248
H3	no/yes no/no	.426ϒ.003 .475ϒ.005	$2x10^{-13}$ $7x10^{-13}$	3.0 0.6	0.68 0.67	-	223 to 293 243 to 297
E3	no/yes	.256ϒ0.19	$2x10^{-18}$	0.7	1.10	+0.5 Pulse	133 to 153
H5	yes/yes	0.637ϒ0.17	$7x10^{-19}$	56.0	0.40	+0.5 Pulse	308 to 353

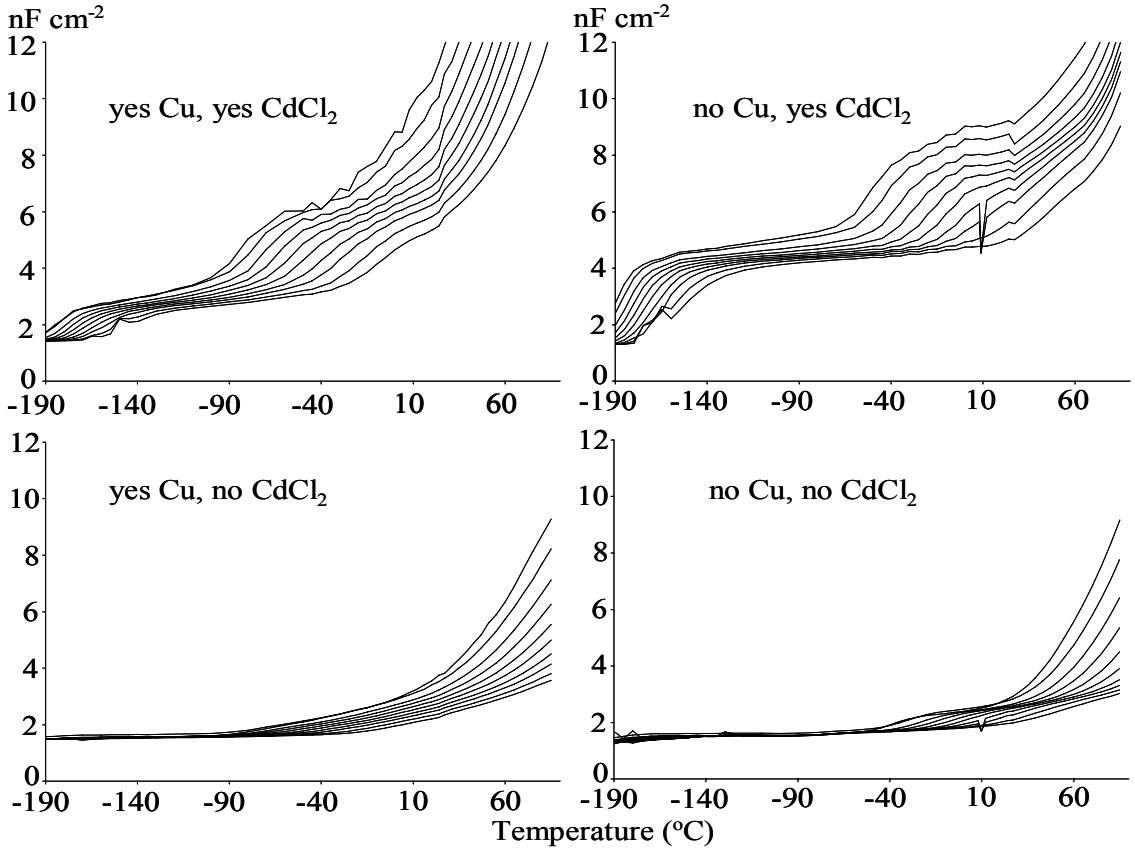

Figure 4.14 C_p versus T for IEC cells. Three detected DES are labeled H1, H2, and H3.

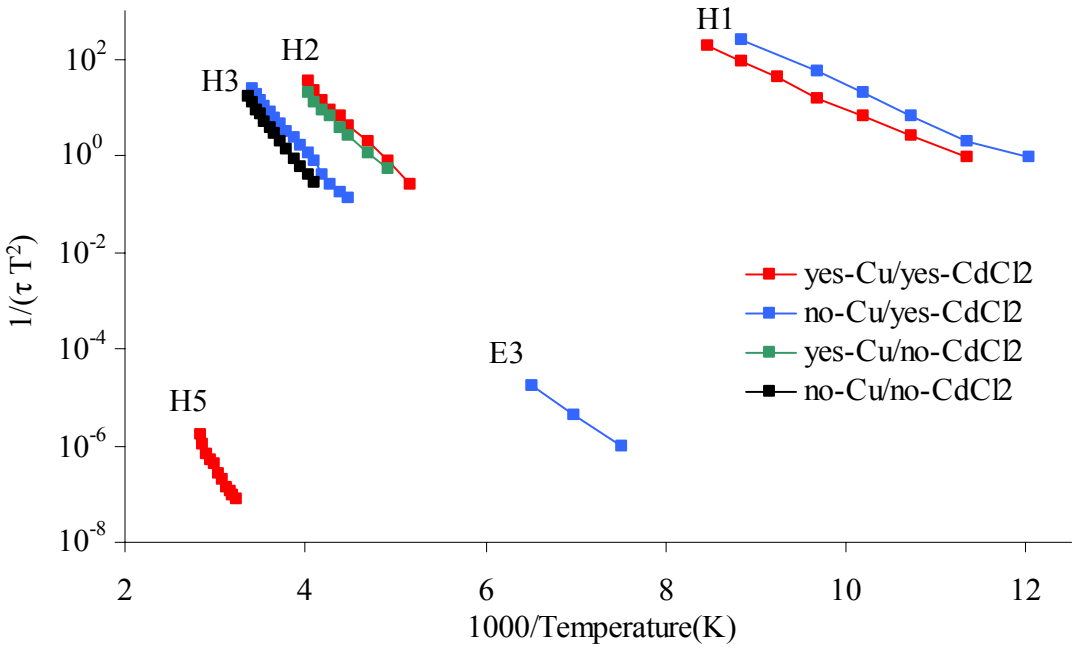

Figure 4.15 Arrhenius plots for IEC cells detected with AS (H1, H2, H3) and CTr (E3, H5).

No H1 signature was detectable in the no-$CdCl_2$ cells. Since H1 has been previously attributed to both the V_{Cd}^{-} and the A-center $V_{Cd}^{2-} - Cl_{Te}^{+}$ defects we can infer that H1 is dominated by $V_{Cd}^{2-} - Cl_{Te}^{+}$ in the yes-$CdCl_2$ cells and that the V_{Cd}^{-} concentration is low in all of the cells. The IEC cells underwent a bromine methanol (BrM) etch which leaves behind a thin Te layer about 1-2nm thick, which contrasts with the NREL cells where an NP etch provides a Te layer hundreds of nm thick. Since the Te layer serves as a V_{Cd}^{-} source, this offers an explanation as to why H1 is not detectable in the no-$CdCl_2$ IEC cells while it is detectable in the no-$CdCl_2$ NREL cells. Also, contrary to Albin's cells, there is no decreasing capacitance with increasing temperature, which indicates that the V_{Cd}^{-} concentration gradient near the back contact is lower than in the NREL cells (see Sec.2), which is consistent with the BrM (not NP) etch treatment.

The H2 defect, which has been attributed to Cu_{Cd}^{-}, has a higher concentration for the yes-Cu/yes-$CdCl_2$ cell than for the yes-Cu/no-$CdCl_2$ cell. Indeed the magnitude of C_t^0 for the former is over 4 times larger than for the latter. The H1 concentration in yes-$CdCl_2$ cells decreases with the addition of Cu which implies that Cu_{Cd} displaces the A center $V_{Cd}^{2-} - Cl_{Te}^{+}$ sites.

The H3 defect also has a higher concentration for the yes-Cu/yes-$CdCl_2$ cell than for the yes-Cu/no-$CdCl_2$ cell implying that $CdCl_2$ contributes to the formation of H3, the attribution of which is still uncertain.

4.3 Cells Fabricated by X. Wu

This section presents the results of studying six cells: three with intentionally added Cu and three without Cu, subjected to three different $CdCl_2$ treatments: (a) 15 min 405^{o}C anneal, (b) 15 min 425^{o}C anneal, and (c) no $CdCl_2$ at all.

The room temperature J-V measurements for these cells with and without Cu and with the three $CdCl_2$ treatments are shown in Table 4.7. The Cu treatment had more impact on cell performance. This contrasts with cells received from D. Albin and B. McCandless where the $CdCl_2$ treatment had the greater impact on performance. In Wu's cells the short circuit dynamic resistance ("shunt resistance") increased with the Cu treatment and this has not been previously typically observed. The 2nd level metrics V_{OC}, J_{SC} and FF were improved by the Cu treatment with

one exception. With the optimal $CdCl_2$ treatment (15' @ 405° C) the no-Cu cell had a better J_{SC}. This has also been observed in the cells from Albin and McCandless.

Table 4.7. J-V characterization results for cells from X. Wu.

Cell	*Treatment*	*Eff* %	V_{oc} *mV*	J_{sc} mA/cm^2	*FF* %	R_{sc} $\Omega - cm^2$	R_{oc} $\Omega - cm^2$
W 1226-2	yes Cu, 15' $CdCl_2$, 405 C	14.06	826	23.7	71.8	1360	2.8
W 1226-8	no Cu, 15' $CdCl_2$, 405 C	7.20	657	24.6	44.5	191	15.4
W 1226-4	yes Cu, no $CdCl_2$	10.44	754	20.9	66.3	491	3.3
W 1226-7	no Cu, no $CdCl_2$	8.47	734	18.9	61.1	369	8.0
W 1226-3	yes Cu, 15' $CdCl_2$, 425 C	10.88	801	23.5	57.8	261	4.9
W 1226-9	no Cu, 15' $CdCl_2$, 425 C ?	2.24	463	14.8	32.7	83	28.3

QE data showed higher near band-gap (~840nm) collection as well as higher blue (~450nm) collection for the high temperature $CdCl_2$ treated cells (15' 425C). This indicates increased CdS/CdTe intermixing and a thinner effective window layer. For the non-$CdCl_2$ treated cells, the QE data showed the least CdS/CdTe intermixing as well as the least collection for wavelengths around 550 nm, which is absorbed in the CdTe near the CdS/CdTe interface.

J-V-T data shows increasing V_{OC} with decreasing temperature. As before a possible explanation for this effect is that the V_{OC} limiting DES are freezing out as the temperature decreases. This effect is less pronounced on the two cells that had the $CdCl_2$ treatment with no Cu. This is consistent with previous observations on cells from Albin, but less so on cells from McCandless. The J-V-T data for J_{SC} shows an abrupt decrease in current collection starting at -120°C for the $CdCl_2$ treated cells. A possible explanation for this is that V_{Cd} and related complex defects with E_a~0.15eV are the dominant dopants in the $CdCl_2$ treated cells and they start freezing out at these temperatures. This is consistent with observations on cells from Albin and McCandless.

A total of twenty detected DES were divided into seven distinct groups based on the DES signatures. The Arrhenius plots for these results are shown in Fig. 4.16. The H1, H2, H3, and H3B signatures at the top of the graph were detected with AS analysis. The E2, E3, and H5 signatures at the bottom of the graph were detected with the CTr analysis. These defect signatures

are in general consistent with those detected in cells supplied by Albin and McCandless although there are some differences in their signatures. A complete listing of the detected defects is in Table 4.8.

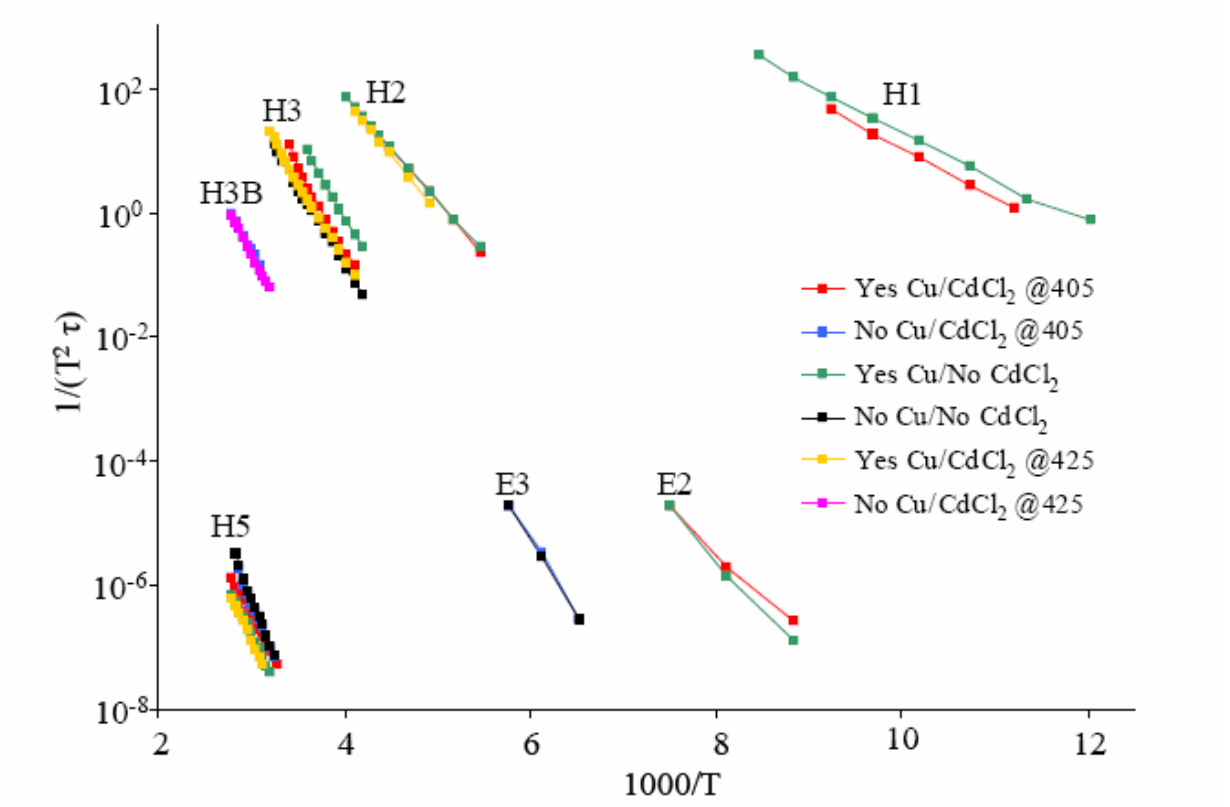

Figure 4.16 Arrhenius plot for DES in the cells produced by Wu and detected with AS (top) and CTr (bottom)

The H1 signature which has been identified as belonging to V_{Cd}^{-} and related complexes had measurable $dC_p / d\ln\omega$ peaks in the cells processed with Cu. For the other cells, while there were no peaks, there were indications that the H1 DES is present with a range of E_a values. This could be a result of the band bending and the AS distortions analyzed in Sec. 2 or it could be an actual band of DES energy levels. Based on the J-V-T data it is possible to conclude that this H1 defect is the dopant that enables superior current collection in the $CdCl_2$ treated cells.

H2, which has been previously identified as Cu_{Cd}^{-}, is only detected in the Cu treated cells. There are not yet experimental indications for what role, if any, this defect might have in superior performance of the Cu treated cells.

The H5 defect is of interest because it has a very strong CTr signature in the cells that have both the Cu and $CdCl_2$ treatments. The magnitude of C_t^0 is an order of magnitude larger than that from any other detected defect, indicating that it has a high concentration. We have also detected H5 with similar magnitudes in the Cu + $CdCl_2$ treated cells from Albin and McCandless. Because of high concentration and position of the level in the bandgap this defect can affect the free carrier concentration (Fermi level) and minority carrier lifetime. So far we refrain ourselves from identifying the defect responsible for the H5 DES.

The minority carrier defect E2 occurs with Cu processing and E3 occurs without Cu. The H3 and H3B occur mostly without the Cu treatment. This is consistent with observations on cells from Albin and McCandless and their impact on cell performance is not known.

Table 4.8. DES signatures determined with AS and CTr in cells produced by X. Wu

DES	Cu/$CdCl_2$	E_a (eV)	σ_a (cm^2)	C_t^0 ($nF\ cm^{-2}$)	Temp range (K)
H1	Yes/405°C	0.16 ±0.01	$5X10^{-13}$	NA	89-108
	Yes/No	0.15 ±0.01	$3X10^{-13}$	1.0	83-118
H2	Yes/405°C	0.34 ±0.01	$2X10^{-13}$	0.4	183-243
	Yes/No	0.33 ±0.01	$1X10^{-13}$	0.7	183-248
	Yes/425°C	0.36 ±0.01	$6X10^{-13}$	0.2	203-243
H3	Yes/405°C	0.54 ±0.03	$7X10^{-12}$	0.6	243-293
	Yes/No	0.52 ±0.02	$9X10^{-12}$	1.0	238-277
	No/No	0.49 ±0.01	$5X10^{-13}$	4.0	238-308
	Yes/425°C	0.50 ±0.01	$8X10^{-13}$	1.0	243-312
H3B	No/405°C	0.54 ±0.05	$1X10^{-14}$	2.0	324-358
	No/425°C	0.57 ±0.02	$4X10^{-14}$	8.0	312-358
E2	Yes/405°C	0.28 ±0.32	$2X10^{-16}$	-0.3	113-133
	Yes/No	0.32 ±0.30	$1X10^{-14}$	-0.8	113-133
E3	No/405°C	0.48 ±0.45	$7X10^{-13}$	-0.1	153-173
	No/No	0.48 ±0.17	$6X10^{-13}$	-0.6	153-173
H5	Yes/405°C	0.55 ±0.01	$2X10^{-20}$	40.0	304-358
	No/405°C	0.71 ±0.05	$1X10^{-17}$	6.0	308-348
	Yes/No	0.60 ±0.02	$9X10^{-20}$	10.0	312-358
	No/No	0.76 ±0.04	$8X10^{-17}$	6.0	308-353
	Yes/425°C	0.63 ±0.02	$2X10^{-19}$	60.0	320-358

5. IMPROVEMENT OF THE CELL PROCESSING

At the start of this work we could reliably produce cells with $\eta > 8\%$ and $V_{OC} > 650 mV$. The studies were undertaken aimed at improvement of the cell performance and optimization of processing procedures.

In all these experiments a 1.5x1.5x1/8 inch TEC-15 glass plate was used as a substrate. Approximately 200nm of CBD CdS was deposited followed by 3-5 microns gas-jet CdTe (the gas-jet system yields a thicker CdTe layer at the center of the plate than at the edges) and $CdCl_2$ anneal. The back contact preparation includes a bromine methanol etch followed by evaporating 10Å of Cu and 500 Å of ZnTe onto the back surface. Then the rapid thermal anneal (RTA) of a back contact structure is applied. The cell is placed in a carbon boat in a bell jar, which is evacuated and back-filled with nitrogen. The boat is heated for 3-5 minutes to drive the Cu into the cell. When the boat temperature reaches the set temperature, the heating element is turned off. Following this, circular gold dots of $0.079 cm^2$ each in a hexagonal pattern are evaporated onto the plate to finish the device. Approximately 50 cells are produced from a single plate.

The first study was aimed at revealing the optimum temperature for the back contact anneal. Following the gold contact deposition, RTA temperatures were applied in succession ranging from $150^o C$ to $400^o C$ in increments of $50^o C$. J-V results averaged from the top 21 cells out of 26 tested are tabulated in table 5.1. The standard deviations are listed to help gage the cell-to-cell non-uniformity within a single plate. The $300^o C$ demonstrated the best performance as well as the least non-uniformity. This was taken as the default RTA temperature for our process. It is evident that the back contact anneal temperature significantly impacts V_{OC} as well as R_{SC}, the short circuit dynamic resistance or "shunt" resistance.

Table 5.1. The effect of the RTA temperature on cell performance

RTA °C	Eff %	V_{OC} mV	J_{SC} mA cm^{-2}	FF %	R_{SC} Ω cm^2	R_{OC} Ω cm^2
None	4.8 ±1.3	500 ±40	20.8 ±3.2	46 ±3	122 ±92	8.5 ±1.4
150	4.8 ±1.7	546 ±33	18.5 ±4.4	47 ±4	148 ±112	9.1 ±1.5
200	5.4 ±1.8	624 ±16	18.7 ±4.3	45 ±5	164 ±124	9.2 ±2.1
250	6.4 ±1.7	672 ±18	20.9 ±2.9	44 ±7	195 ±141	8.7 ±2.1
300	8.2 ±0.6	660 ±13	23.1 ±0.4	53 ±3	530 ±150	9.9 ±2.3
350	6.3 ±1.6	609 ±100	22.7 ±0.7	45 ±7	316 ±106	22.8 ±12.2
400	3.9 ±1.4	570 ±89	21.4 ±1.2	32 ±8	197 ±129	99.2 ±82.4

A J-V graph of for a single cell over the range of RTA temperatures is shown in Fig. 5.1. For the "under-annealed" $250^{o}C$ cell a voltage dependent current collection is evident. This could indicate a weak electric field or lateral non-uniformity with weak diodes. For the "over-annealed" $350^{o}C$ cell the rollover is similar to that of severely degraded cells.

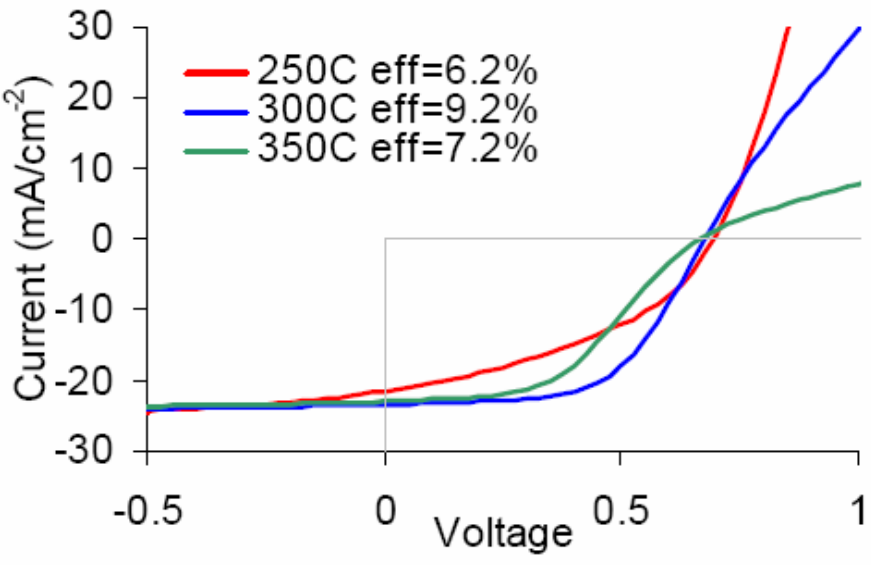

Figure 5.1. J-V curves for RTA temperatures bracketing the optimum efficiency.

After that study a number of changes in the CdTe cell growth recipe were tested. One was changing the CdS deposition technique from Chemical Bath Deposition (CBD) to thermal evaporation. The ability to deposit the CdS layer by thermal evaporation at CSM was recently developed. We have suspected that microscopic bubbles or contaminant particles with the CBD

CdS deposition have been leading to the visible pinholes seen later in processing that are believed to cause performance degradation. With the thermally evaporated CdS the visible pinholes have been virtually eliminated.

Another performance enhancement was discovered while using nitrogen as the gas-jet VTD carrier gas instead of helium. The nitrogen was initially used in place of helium to calibrate the gas-jet source and chamber pressures, which are measured with thermocouple gauges that are known to give distorted readings with helium. During this process it was found that the nitrogen carrier gas improved cell performance.

The effects of these two changes on the cell performance can be seen in Fig. 5.2.

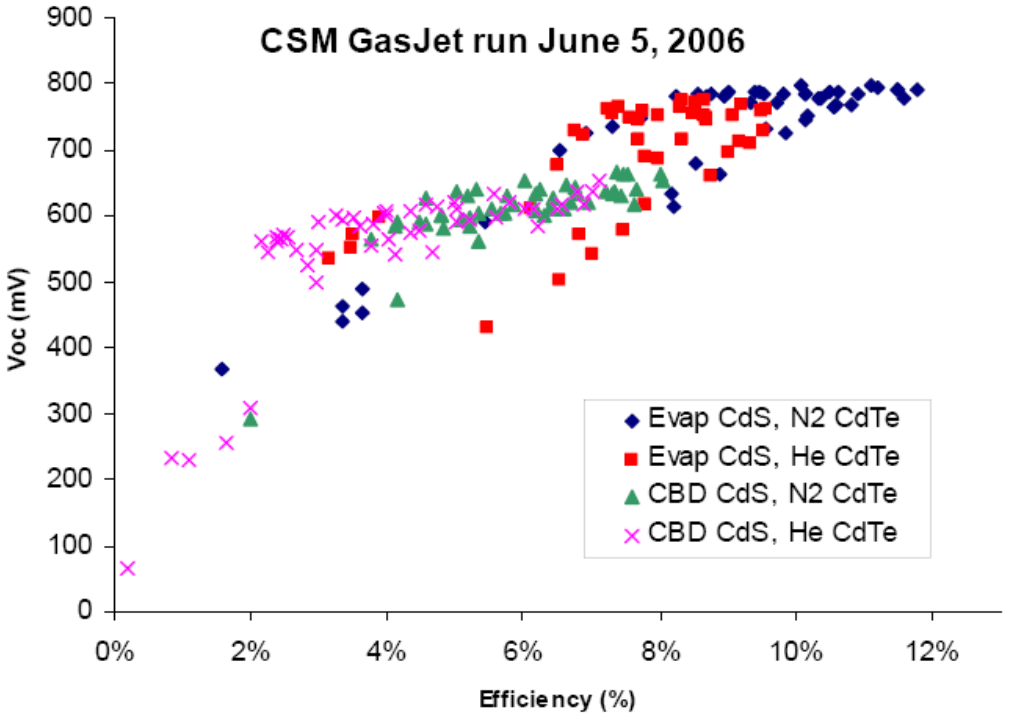

Fig. 5.2 Open circuit voltage versus cell efficiency. Dot cells 0.079 cm^2 each, were processed with CBD or evaporated CdS, and CdTe deposited in gas-jet system with nitrogen or helium carrier gas.

Each of the four categories in Figure 5.2 consists of approximately 50 dot cells each 0.079 cm^2 on a 1.5"x1.5" panel. The improved V_{OC} with the evaporated CdS layer is evident. The improved efficiencies with the N_2 carrier gas are due to a combination of better V_{OC} and fill factor.

These and other experiments led to the production of a record for the CSM gas-jet VTD system cell with $\eta = 12.6\%$, $V_{OC} = 797\,mV$, $J_{SC} = 23.3\,mA/cm^2$, and $FF = 68\%$. It should be noticed that the cell had no front contact buffer layer, antireflection coating, etc. As mentioned previously, our J-V characterization underestimates cell efficiency due to discrepancy between the solar spectrum and that of our light source.

These highest performing cells were produced with the following processing steps:

- Began with commercial TEC15 soda lime glass coated with a fluorine doped tin-oxide.
- Detergent clean that included a UV/ozone step to remove residual organics.
- 200nm of CdS vacuum evaporated onto the substrate with $T_{substr.} = 150^o C$.
- $\sim 4\,\mu m$ CdTe deposited by gas-jet with a N_2 carrier gas, a nominal substrate temperature of $375^o C$, a quartz frit orifice temperature of $775^o C$ and a source temperature of $700^o C$.
- $CdCl_2$ topically applied from an ultrasonic nebulizer mist of 1 mole $CdCl_2$ solution in a heated chamber.
- Annealed in a 50/50 oxygen/nitrogen atmosphere at $400^o C$ for 35 minutes.
- 2nm of Cu followed by 50nm ZnTe thermally evaporated onto room temperature substrate.
- Rapid Thermal Anneal to $280^o C$ to activate the back contact.
- $0.079\,cm^2$ gold back contact dots deposited by thermal evaporation onto room temperature substrate.
- Manual scribe along edge to front contact and application of indium by soldering.
- The perimeter of the dot cell itself was also scribed in order to minimize edge current collection that could artificially inflate the measured current and J_{sC}.

6. REFERENCES

1. "Studies of Basic Electronic Properties of CdTe-Based Solar Cells and Their Evolution During Processing and Stress", V. Kaydanov and T.R. Ohno, Final Technical Report , Oct.16, 2001- Aug. 31, 2005, Subcontract No.ADJ-2-30630-05 under Prime Contract No. DE-AC36-99-GO10337, Colorado School of Mines, Golden CO, 2005

2. Blood, P., Orton, J.W., The electrical characterization of semiconductors: majority carriers and electron states, Academic Press Limited, London, 1992

3. Meyer, W., Neldel, H., *Z. Tech. Phys.* (Leipzig) 12, 588, 1937

4. Widenhorn, R., Rest, A., Bodegom, E., "The Meyer–Neldel rule for a property determined by two transport mechanisms", *J. Appl. Phys.* Vol **91**, (10), pp. 6524-6528, May 15, 2002

5. M. Burgelman, P. Nollet and S. Degrave, "Modeling polycrystalline semiconductor solar cells", *Thin Solid Films*, **361-362**, 527-532, 2000

6. Gloeckler, M., Fahrenbruch. A.L., and Sites, J.R., "Numerical Modeling of CIGS and CdTe Solar Cells: Setting the Baseline", Presented at the *World Conference on Photovoltaic Energy Conversion*, Tokyo, Japan, May, 2003

7. Fahrenbruch, A., Modeling Results for CdS/CdTe Solar Cells, CSU Report, http://www.physics.colostate.edu/groups/photovoltaic/PDFs/ModCdTe.pdf, March 2000

8. F.H. Seymour, "Studying of Electronic States controlling the Performance of CdTe Solar Cells", Ph.D. Thesis, September 2005, Colorado School of Mines, Golden, CO

9. McCandless, B., Sites, J. R., in Handbook of Photovoltaic Science and Engineering, edited by A. Luque and S. Hegedus, John Wiley & Sons Ltd, West Sussex, England, ch. 14, pp 617-657, 2003

10. Castaldini, A., Calvallini, A., Fraboni, B., Fernandez, P., Piqueras, J. , "Deep energy levels in CdTe and CdZnTe", *J. Appl. Phys*., **83** No 4 p212-2126, 1998

11. Hofmann, D.M., Omling, P., Grimmeiss, H.G., Meyer, B.K., Benz, K.W., Sinerius, D. "Identification of the chlorine A center in CdTe", Phys. Rev. B **45** 11, pp 6247-6250, 1992

12. Albin, D., Dhere, R., Wu, Z., Gessert, T., Romero, M.J., Yan, Y., Asher, S. "Perturbation of Copper Substitutional Defect Concentration in CdS/ CdTe Heterojunction Solar Cell Devices", *Proceedings of the Materials Research Society Conference, Symposium F*, San Francisco, California, USA, April, 2002

13. Zanio, Kenneth, Semiconductors and Semimetals Volume 13 Cadmium Telluride, Academic Press, New York, USA, p162, 1978

14. Balcioglu, A., Ahrenkiel, R.K., Hasoon, F., "Deep-level impurities in CdTe/CdS thin-film solar cells", J. Appl. Phys., **88** No 12 p7175-7178, 2000

15. Wei, S. H., Zhang, S. B., “Chemical trends of defect formation and doping limit in II-IV semiconductors: the case of CdTe”, Phys. Rev. B **66**, p155211, 2002

16. Feldman, S.D., Collins, R.T., Kaydanov, V., Ohno, T.R., “Effects of Cu in CdS/CdTe solar cells studied with patterned doping and spatially resolved luminescence”, *Appl. Phys. Lett*., **85** (9), 1529-1531, 2004

17. Xuanzhi Wu, “High-efficiency polycrystalline CdTe thin-film solar cells”, *Solar Energy*, 77 (2000), 803-814

7. APPENDICES

7.1 Personnel

The names, titles, and representative responsibilities of the individuals contributed to this work are presented below.

Timothy R. Ohno, Associate Professor of Physics: Photovoltaic Development, Surface Physics, Electroluminescence, Principal Investigator

Fred H. Seymour, Post Doc. Fellow: Photovoltaic Development; Cell Processing and Characterization; Studying of Deep Electronic States by means of Admittance Spectroscopy and Transients; Modeling of Cell characteristics with AMPS and SCAPS; Developing of Database

Joe Beach, Assistant Research Professor: Photovoltaic Development, Developing Novel Approaches to the Cell Processing; Design and Assembling Processing Equipment; J-V Characterization of Cells and the Data Analysis

Victor I. Kaydanov, Research Professor of Physics: Photovoltaic Development; Studying of the Defect Electronic States

7.2 Laboratory Improvements

The principal change in the laboratory during this period was modification of the thermal evaporation system that had previously been used for back contact preparation. The evaporator was modified to permit rapid change-out of evaporation source material, including CdS and CdTe for the studies cited above, and sample heating during deposition. As a result of the evaporation of Cd-containing compounds a barrier system with venting through a HEPA filter was constructed. The system was tested by CSM Environmental Health and Safety to verify that no cadmium contamination resulted.

7.3 Publications/Presentations

1. "Simulated Admittance Spectroscopy of High Concentration Deep Level Defects in CdTe Thin-Film Solar Cells", F. H. Seymour, V. Kaydanov, T. R. Ohno, J. Appl. Phys., **100**, 033710, August 8, 2006.

2. "Admittance Spectroscopy Characterization of Deep Electronic States in Cadmium Telluride Solar Cells", F. H. Seymour, V. Kaydanov, T. R. Ohno, Proceedings from 2006 IEEE World Conference on Photovoltaics Energy Conversion, Waikoloa, Hawaii, May, 2006.

3. Organized and facilitated V_{OC} mini-workshop at National CdTe team meeting, Golden, Colorado, March 10, 2006 (description in Q2 report).

4. "Performance and defects in CSS and VTD CdTe cells treated with and without Cu and $CdCl_2$", F.H. Seymour, V. Kaydanov, T.R. Ohno, Presentation at National CdTe team meeting, Golden, Colorado, March 9, 2006.

5. "Deep Electronic States in CdTe Solar Cells Detected with Admittance Techniques", F. H. Seymour, V. Kaydanov, T. R. Ohno, DOE Solar Energy Technologies Program 2005 Review Meeting, Denver, Colorado, November, 2005.

6. "Studies of Electronic States Controlling the Performance of CdTe Solar Cells", F. H. Seymour, Ph.D. thesis, Colorado School of Mines, October, 2005.

7. "Cu and $CdCl_2$ Influence on Defects Detected in CdTe Solar Cells with Admittance Spectroscopy", F. H. Seymour, V. Kaydanov, T. R. Ohno, D. Albin, Appl. Phys. Lett., Vol 87, 153507, October, 2005.

REPORT DOCUMENTATION PAGE

Form Approved
OMB No. 0704-0188

PLEASE DO NOT RETURN YOUR FORM TO THE ABOVE ORGANIZATION.

1. REPORT DATE *(DD-MM-YYYY)*	2. REPORT TYPE	3. DATES COVERED *(From - To)*
January 2007	Subcontractor Report	01 November 2005-31 October 2006

4. TITLE AND SUBTITLE
Studies of Basic Electronic Properties of CdTe-Based Solar Cells and Their Evolution During Processing and Stress: Annual Technical Report, 01 November 2005 – 31 October 2006

5a. CONTRACT NUMBER
DE-AC36-99-GO10337

5b. GRANT NUMBER

5c. PROGRAM ELEMENT NUMBER

6. AUTHOR(S)
J. Beach, F.H. Seymour, V.I. Kaydanov, and T.R. Ohno

5d. PROJECT NUMBER
NREL/SR-520-41097

5e. TASK NUMBER
PVB75201

5f. WORK UNIT NUMBER

7. PERFORMING ORGANIZATION NAME(S) AND ADDRESS(ES)
Physics Department
Colorado School of Mines
Golden, Colorado 80401

8. PERFORMING ORGANIZATION REPORT NUMBER
ADJ-2-30630-05

9. SPONSORING/MONITORING AGENCY NAME(S) AND ADDRESS(ES)
National Renewable Energy Laboratory
1617 Cole Blvd.
Golden, CO 80401-3393

10. SPONSOR/MONITOR'S ACRONYM(S)
NREL

11. SPONSORING/MONITORING AGENCY REPORT NUMBER
NREL/SR-520-41097

12. DISTRIBUTION AVAILABILITY STATEMENT
National Technical Information Service
U.S. Department of Commerce
5285 Port Royal Road
Springfield, VA 22161

13. SUPPLEMENTARY NOTES
NREL Technical Monitor: Harin S. Ullal

14. ABSTRACT *(Maximum 200 Words)*

We describe the results of our continuing study of deep electronic states controlling open-circuit voltage in CdTe/CdS thin-film solar cells (Task 1). The study includes: (1) analysis of factors affecting trap signatures derived from admittance spectroscopy and capacitance transients measurements, such as activation-energy capture cross-sections and trap-density estimates, and (2) comparative studies of cells received from four different sources and prepared with significant variations in cell structure and processing procedures.

15. SUBJECT TERMS
Admittance spectroscopy; capacitance transients; deep electronic states; chemical-bath deposition; post-deposition annealing; gas-transport deposition; Gas-Jet system; optimization;

16. SECURITY CLASSIFICATION OF:			17. LIMITATION OF ABSTRACT	18. NUMBER OF PAGES	19a. NAME OF RESPONSIBLE PERSON
a. REPORT	b. ABSTRACT	c. THIS PAGE			
Unclassified	Unclassified	Unclassified	UL		19b. TELEPHONE NUMBER (*Include area code*)

Standard Form 298 (Rev. 8/98)
Prescribed by ANSI Std. Z39.18